3'UTR-directed, kinase proximal mRNA decay inhibits C/EBPβ phosphorylation/activation to suppress senescence in tumor cells

Jacqueline Salotti[1], Baktiar Karim[2], Sweta Misra[1], Linshan Hu[1], Srikanta Basu[1], Nancy Martin[1], Brian T. Luke[3], Karen Saylor[4], Thorkell Andresson[5], David A. Scheiblin[6], Stephen Lockett[6], Lino Tessarollo[1], and Peter F. Johnson[1]*

[1]Mouse Cancer Genetics Program, Center for Cancer Research, National Cancer Institute, Frederick, Maryland, USA; [2]Molecular Histopathology Laboratory, Laboratory Animal Sciences Program, Frederick National Laboratory for Cancer Research, Frederick, MD; [3]Advanced Biomedical Computational Science, Frederick National Laboratory for Cancer Research, Frederick, MD, USA; [4]Laboratory Animal Sciences Program, Frederick National Laboratory for Cancer Research, Frederick, MD, USA; [5]Protein Characterization Laboratory, Cancer Research Technology Program, Frederick National Laboratory for Cancer Research, Leidos Biomedical Research, Inc., Frederick, Maryland, USA; [6]Optical Microscopy and Image Analysis Laboratory, Cancer Research Technology Program, Frederick National Laboratory for Cancer Research, Frederick, Maryland, USA

***corresponding author**

Abstract

C/EBPβ is a potent regulator of RAS-induced senescence (RIS) and the SASP. C/EBPβ is post-translationally activated in RIS cells by the effector kinases ERK1/2 and CK2, but in tumor cells activation is suppressed by the *CEBPB* 3'UTR. 3′UTR regulation of protein activity (UPA) requires a G/U-rich element (GRE) and its cognate binding protein, HuR. These components segregate *CEBPB* transcripts away from a perinuclear compartment harboring ERK1/2 and CK2, restricting C/EBPβ from its activating kinases. We report here that the mRNA decay proteins UPF1 and Staufen1/2 are essential UPA factors enriched within the perinuclear cytoplasm. STAU1/2 colocalize with CK2 on perinuclear signaling endosomes where they promote localized *CEBPB* mRNA decay. UPF1 or STAU1/2 depletion in tumor cells increased *CEBPB* transcripts adjacent to CK2 foci, coinciding with C/EBPβ activation and senescence. The GRE and an adjacent STAU binding site act to suppress C/EBPβ-mediated senescence, while a separate 3'UTR region inhibits SASP induction. Accordingly, $Kras^{G12D}$-driven lung tumors in mice carrying a *Cebpb* GRE deletion rarely progressed to malignant adenocarcinomas. Our findings identify kinase-proximal mRNA decay as a novel mechanism to inhibit C/EBPβ activating modifications in tumor cells to facilitate senescence bypass.

Introduction

Senescence is a persistent state of cell cycle arrest elicited by stress stimuli such as DNA damage, oxidative stress and oncogenes (He and Sharpless, 2017). Oncogene-induced senescence (OIS) triggered by activated *RAS*, *BRAF*, *MYC* or other oncogenes establishes an intrinsic barrier to neoplastic transformation and cancer (Braig and Schmitt, 2006). The OIS checkpoint imposes selective pressure for mutations or epigenetic events that disable key pro-senescence pathways such as ARF-p53 and p16-RB, allowing premalignant cells to bypass senescence and progress to a fully transformed state. Senescent cells also express a characteristic set of secreted proteins, collectively termed the senescence-associated secretory phenotype (SASP) (Coppe et al., 2010) primarily composed of pro-inflammatory cytokines, their receptors and matrix proteases. SASP factors reinforce and propagate senescence through autocrine and paracrine mechanisms (Acosta et al., 2013; Hoare et al., 2016; Kuilman et al., 2008). SASP cytokines released by senescent cells also signal for clearance by the immune system, and this senescence surveillance process is critical for efficient tumor suppression *in vivo* (Kang et al., 2011).

NF-κB and C/EBPβ are the primary transcriptional regulators of the SASP in senescent cells (Acosta et al., 2008; Herranz and Gil, 2018; Kuilman et al., 2008; Lopes-Paciencia et al., 2019; Salotti and Johnson, 2019). By contrast, tumor cells typically display relatively low expression of SASP genes. This “cold” inflammatory profile may contribute to the cells’ ability to evade immune surveillance. Paradoxically, many cancer cells contain activated NF-κB and express C/EBPβ, which would be expected to induce the SASP. However, the pro-senescence function of C/EBPβ is inhibited in tumor cells by a 3'UTR-dependent mechanism that blocks RAS-induced post-translational activating modifications (Basu et al., 2018b; Basu et al., 2011). The 3'UTR also potently suppresses the transcriptional activity of C/EBPβ toward SASP genes. This 3'UTR

regulation of protein activity (UPA) mechanism involves subcellular partitioning of *Cebpb* transcripts, excluding them from a perinuclear cytoplasmic region containing the C/EBPβ activating kinases ERK1/2 and CK2. Thus, C/EBPβ cannot access its kinases, suppressing phosphorylation on C/EBPβ residues Thr188 (ERK1/2) and Ser222 (CK2) and possibly other sites (Basu et al., 2018b; Basu et al., 2011). This, in turn, restrains the increased DNA binding, homodimerization and transcriptional potential of C/EBPβ that determine its cytostatic and SASP-inducing activities in senescent cells (Basu et al., 2018b; Huggins et al., 2013; Lee et al., 2010; Sebastian et al., 2005).

UPA is abrogated in primary cells undergoing oncogenic RAS-induced senescence (RIS), allowing C/EBPβ to become activated by senescence stimuli. UPA is disabled by a RAS-CaMKKβ-AMPK pathway that induces nuclear translocation of HuR/ELAVL1 (Basu et al., 2018a), an RNA-binding protein that recognizes a G/U-rich element (GRE) region in the *Cebpb* 3'UTR (Basu et al., 2011; Gantt et al., 2005). HuR and the GRE motif are both required for C/EBPβ UPA, as HuR ablation or deletion of the GRE abrogate 3'UTR inhibition and disrupt peripheral *Cebpb* mRNA localization (Basu et al., 2011). Cytoplasmic HuR levels are elevated in tumor cells and promote increased tumor malignancy (Lopez de Silanes et al., 2005) by facilitating unrestrained proliferation and senescence bypass through various target mRNAs, including repressing C/EBPβ through the UPA mechanism. HuR binds up to 50% of mammalian mRNAs (Lebedeva et al., 2011) and can regulate diverse aspects of RNA and protein biogenesis, such as nuclear-cytoplasmic mRNA transport, mRNA stability and translation efficiency. The precise role of HuR in C/EBPβ UPA and the mechanism by which the 3'UTR controls *Cebpb* mRNA localization are important but unresolved questions. Since HuR alone is unlikely to establish

C/EBPβ UPA, we sought to characterize other components of the UPA machinery to gain further insights into the underlying mechanism.

Results

Identification of *Cebpb* GRE-associated proteins

We hypothesized that a higher-order protein complex assembles on the GRE:HuR scaffold to establish UPA and inhibit C/EBPβ activity (Fig. 1A). To identify novel *Cebpb* GRE-interacting factors, we used an *in vitro* RNA affinity purification/mass spectrometry (MS) procedure previously employed to characterize proteins that bind to A/U-rich elements (AREs) (Butter et al., 2009) (Fig. S1A). Proteins associating with the 102 nt *Cebpb* GRE sequence were purified from cytoplasmic lysates of NIH 3T3 fibroblasts, as these cells are UPA proficient and therefore express the relevant factors. Specific enrichment was determined by comparing GRE-bound proteins to those interacting with a control GFP RNA of similar length. A Coomassie stained protein gel revealed ~50 visible bands enriched in the *Cebpb* GRE-bound fraction (Fig. 1B). Proteins from three independent pull-down experiments were then analyzed by mass spectrometry. GRE binders were distinguished from non-specific background by calculating GRE:GFP peptide ratios. Using a threshold of $\log_2$ GRE:GFP ratio ≥1; $-\log_{10}$ FDR ≥1, 324 GRE-interacting proteins were identified (Fig. 1C). The GRE-bound protein list was analyzed by gene ontology (DAVID, GOTERM_BP) (Sherman et al., 2022) to identify enriched biological processes (Fig. 1D). As expected, the categories were skewed toward RNA-associated functions such as translation, splicing and RNA decay.

As a secondary screen for functional UPA proteins, we used RNAi to deplete a set of 21 prominent GRE interactors (ranked by peptide ratios) as well as other candidates identified in a

pilot GRE pull-down experiment. We then examined expression of several C/EBPβ-regulated SASP genes, reasoning that depletion of bona fide UPA proteins should activate C/EBPβ and induce their transcription. These tests were performed in $HRAS^{G12V}$-tranformed NIH 3T3 cells transduced with a *Cebpb*^{UTR} construct (denoted $3T3^{RAS}$-β^{UTR}), since $3T3^{RAS}$ cells express low levels of endogenous C/EBPβ (Sebastian and Johnson, 2009). The same knockdowns were performed in $3T3^{RAS}$ cells carrying a C/EBPβ shRNA construct to further deplete endogenous C/EBPβ. As shown in Figs. S1B and 1E, *Il6*, *Il1α*, *Cxcl1* and *Ccr1* mRNAs were increased upon knockdown of Strbp and UPF1 (RENT1) in $3T3^{RAS}$-β^{UTR} cells but not in $3T3^{RAS}$-sh*Cebpb* cells. Depletion of certain other candidates, such as Elavl1 (HuR) and Fubp3, also induced *Ccr1* expression but did not appreciably activate the other SASPs. These data implicate UPF1 and Strbp as potential components of the UPA system.

UPF1 is an RNA helicase/ATPase and RNP remodeling protein that is a key regulator of nonsense-mediated mRNA decay (NMD) and other RNA degradation pathways (Kurosaki and Maquat, 2016). We further investigated the role of UPF1 in C/EBPβ UPA for several reasons: 1) UPF1 appeared as a high-ranking hit in the GRE interaction screen and, among the UPA candidates tested, UPF1 depletion caused the largest induction of SASP genes (Fig. S1B); 2) UPF1 was found to bind *Cebpb* transcripts in genome-wide CLIP-seq studies of RNA:protein interactions (Li et al., 2014); 3) a published database of RNA-independent and -dependent Upf1-interacting proteins (Flury et al., 2014) overlapped considerably with our list of GRE binders; 4) UPF1 displays synthetic lethality with oncogenic RAS in tumor cells (Luo et al., 2009), consistent with our prediction that shRNAs disrupting C/EBPβ UPA would be deleterious to the proliferation/survival of RAS-transformed cells.

We confirmed that UPF1 depletion activates SASP genes in a C/EBPβ-dependent manner in $3T3^{RAS}$ cells (Fig. 1E) and used immunoblotting to verify selective enrichment of UPF1 and HuR in the GRE-bound protein fraction (Fig. 1F). Native RNA immunoprecipitation (nRIP) demonstrated that UPF1 and HuR associate with *Cebpb* transcripts in NIH 3T3 cells (Fig. 1G). To determine whether interaction of UPF1 and HuR with *Cebpb* mRNA requires the GRE, we performed nRIP using $HRAS^{G12V}$-transformed MEFs that carry a deletion of the *Cebpb* GRE ($p19^{Arf-/-};GRE^{\Delta/\Delta}$ cells; see below). HuR binding to *ΔGRE* transcripts was greatly reduced compared to *WT* mRNAs (Fig. S1C). However, UPF1 binding was not decreased, indicating that it can be recruited to *Cebpb* mRNAs through additional mechanisms. To test whether UPF1 and HuR interact, we performed co-immunoprecipitation assays using NIH 3T3 cell lysates. As shown in Fig. 1H, HuR and UPF1 showed reciprocal co-immunoprecipitation and this interaction was disrupted by addition of RNase, indicating that the two proteins associate in an RNA-dependent manner. These findings are consistent with proteomic data identifying HuR as an RNA-dependent UPF1 interactor (Flury et al., 2014).

Perinuclear Upf1-dependent mRNA decay controls partitioning of *CEBPB* transcripts

To investigate if UPF1 contributes to UPA-mediated inhibition of C/EBPβ activity, we first examined the subcellular distribution of *Cebpb* transcripts and UPF1 in NIH 3T3 cells. RNA FISH labeling showed exclusion of *Cebpb* mRNAs from the perinuclear region (Fig. S2A), as observed previously (Basu et al., 2018a). Interestingly, UPF1 was restricted to the perinuclear area that was largely devoid of *Cebpb* FISH signals. When UPF1 was depleted, *Cebpb* transcripts became more abundant in this region. This effect was particularly evident in individual cells displaying efficient knockdown of Upf1.

NIH 3T3 cells are not transformed and hence do not display constitutive perinuclear localization of CK2 and p-ERK (Basu et al., 2018b), and the elongated spindle morphology of RAS-transformed NIH 3T3 cells makes determination of subcellular partitioning difficult. Therefore, to investigate the spatial relationship between *CEBPB* mRNA and kinases we analyzed human A549 lung adenocarcinoma cells ($KRAS^{G12S}$). Immunofluorescence imaging showed that UPF1 was perinuclear in these cells, as was CK2α, and both proteins were largely non-overlapping with *CEBPB* transcripts (Fig. 2A). Fluorescently tagged UPF1 and CK2α proteins were also perinuclear in live A549 cells and the signals partially overlapped (Fig. 2B). Notably, UPF1 depletion increased the abundance of nuclear proximal *CEBPB* transcripts (Fig. 2A). To quantify this effect, we used CK2α signal thresholding to define a perinuclear kinase region and determined the percentage of *CEBPB* FISH signals within the CK2 boundary (Fig. 2C). mRNA-CK2 overlap averaged 25.6% in control cells but increased to 62.6% when UPF1 was depleted ($p<0.0001$).

As UPF1 plays a key role in NMD, its restriction to perinuclear areas that are devoid of *CEBPB* transcripts suggested that localized decay may prevent mRNA accumulation in these regions. Supporting this idea, depletion of UPF1 or HuR in A549 cells increased the overall abundance of *CEBPB* mRNAs, as determined by RT-qPCR assays (Fig. 2D) and quantitation of mRNA FISH signals (Fig. S2B). Similar results were seen in a panel of RAS-transformed fibroblasts and human tumor cells (Fig. S2C). The increase in *CEBPB* levels in UPF1-depleted cells was associated with an extension of *CEBPB* mRNA half-life (Fig. 2E). A similar stabilization was seen upon HuR silencing, which triggers perinuclear localization of *CEBPB* transcripts (Basu et al., 2011). These observations indicate that UPF1 and HuR promote perinuclear mRNA decay (PMD).

During NMD, UPF1 activity is stimulated through phosphorylation on Ser1127 by the SMG1 kinase (Kurosaki and Maquat, 2016). This modification initiates recruitment of SMG6, an endonuclease that cleaves the target transcript, and other NMD components such as SMG5/7 which trigger de-capping, de-adenylation, and exonucleolytic mRNA degradation. We depleted SMG1, SMG5, SMG6 and SMG7 in A549 cells to evaluate their involvement in localized *CEBPB* mRNA decay. Neither SMG1 nor SMG5 silencing appreciably altered *CEBPB* mRNA exclusion from the CK2-rich perinuclear region (Fig. S2D-E), although SMG1 silencing led to the expected decrease in UPF1 Ser1127 phosphorylation (Fig. S2F). By contrast, SMG6 and SMG7 knockdown caused a clear increase in perinuclear mRNA abundance (Fig. 2F-G), indicating that these two factors contribute to *CEBPB* PMD.

UPF1 suppresses C/EBPβ phosphorylation and senescence in tumor cells

The segregation of *CEBPB* transcripts from perinuclear CK2 in tumor cells inhibits C/EBPβ phosphorylation on a CK2 site (Ser222 in mouse, Ser271 in human) that stimulates C/EBPβ DNA binding and pro-senescence activity (Basu et al., 2018b). Super-resolution imaging of A549 cells depleted for UPF1 revealed that many *CEBPB* transcripts became closely opposed to CK2α foci (Fig. 3A). These CK2 foci correspond to perinuclear signaling endosomes (Basu et al., 2018b). Proximity labeling assays (PLA) similarly showed increased association between C/EBPβ and CK2α in UPF1 knockdown cells compared to a control ($p=0.0002$), demonstrating that the protein is also present at these locations, at least transiently prior to nuclear translocation. This suggests that when UPA-dependent mRNA decay is interrupted, C/EBPβ becomes phosphorylated by CK2 through targeting of *CEBPB* transcripts to signaling endosomes. As we were unable to generate an antibody that efficiently detects human C/EBPβ p-Ser271, we used a p-Ser222 antibody to monitor

phosphorylation of mouse C/EBPβ in the chromatin fraction of $3T3^{RAS}$-β^{UTR} cells. UPF1 depletion augmented p-Ser222 levels (normalized to total C/EBPβ) by 4.6-fold (Fig. 3C) and increased C/EBPβ DNA binding by up to 8-fold (Fig. 3D). UPF1 silencing also severely reduced colony formation, which was partially ameliorated in cells depleted for C/EBPβ (Figs. 3E and S3A). Enhanced C/EBPβ DNA binding was also observed upon UPF1 knockdown in PANC-1 PDAC cells and HRAS-transformed, *p19*^{Arf}-deficient MEFs (Fig. S3B). Thus, UPF1 is required to inhibit C/EBPβ phosphorylation/activation in transformed cells.

UPF1 depletion in $3T3^{RAS}$-β^{UTR} cells potently induced senescence (SA-βGal positivity) in a C/EBPβ-dependent manner (Fig. 3F). Similar results were obtained using a panel of human tumor cells and transformed MEFs (Fig. S3C). Furthermore, SASP genes were strongly up-regulated after UPF1 ablation in transformed cells (Figs. 3G and S3D). A549 cells lacking UPF1 were also unable to form lung tumors after intravenous injection into immune-deficient mice (Fig. 3H). Hence, tumor cells require UPF1 to suppress senescence and promote tumorigenesis, at least partly by inhibiting C/EBPβ activity. UPF1 was markedly down-regulated in senescent human IMR90 fibroblasts and *WT* MEFs expressing $HRAS^{G12V}$ while being maintained in a subset of RAS-transduced *p19*$^{Arf-/-}$ MEF cells (Fig. S3E), consistent with its role in inhibiting senescence.

To more directly address whether mRNA decay is critical for subcellular partitioning of *CEBPB* transcripts, we generated mouse *Cebpb* constructs containing the triple helical RNA stability element from *Malat1* (Wilusz et al., 2012) or a scrambled version of this sequence (Scrbl) inserted at the 3' end of the 3'UTR. These genes, together with *Cebpb*^{UTR} (WT) and *Cebpb*$^{\Delta UTR}$ controls, were expressed in A549 cells. FISH labeling of transcripts using a probe that detects only murine *Cebpb*, together with CK2α IF, showed perinuclear exclusion of the *Cebpb*^{UTR} and *Cebpb*^{Scrbl} transcripts (Fig. 3I). However, *Cebpb*$^{\Delta UTR}$ and *Cebpb*^{Malat1} mRNAs displayed

perinuclear clustering and increased overlap with CK2α. *Cebpb*$^{\Delta UTR}$ and *Cebpb*^{Malat1} also increased the proportion of senescent cells, in contrast to *Cebpb*^{UTR} and *Cebpb*^{Scrbl} which maintained a basal level of senescence (Fig. 3J). Thus, the *Malat1* RNA stability element can override 3'UTR inhibition, providing additional evidence that localized mRNA decay is essential to limit C/EBPβ synthesis in the kinase-rich perinuclear region and suppress its activation.

Staufen RNA-binding proteins are essential for *CEBPB* PMD

The double-stranded RBPs, Staufen1 and 2, were enriched in the GRE pull-down fraction, as confirmed by immunoblotting (Fig. 4A). STAU proteins control mRNA decay and localization (Park and Maquat, 2013), STAU-mediated mRNA decay (SMD) requires UPF1 (Kim et al., 2005), and STAU2 depletion is synthetically lethal with mutant *KRAS* in colorectal cancer cells (Luo et al., 2009). Therefore, we sought to investigate their possible connection to PMD. Stau1 and 2 associated with *Cebpb* transcripts in NIH 3T3 cells (Fig. 4B) and interacted with HuR and Upf1 in an RNA-dependent manner (Fig. S4A). In addition, fluorescently tagged STAU1 and 2 expressed in A549 cells were concentrated in perinuclear regions that contain UPF1 (Fig. 4C). This was corroborated by IF/RNA FISH imaging, which further demonstrated that areas of STAU1/2 and UPF1 correlate with exclusion of *CEBPB* mRNA (Fig. 4D).

These results suggest that STAU1/2 might control perinuclear *CEBPB* mRNA decay. Depletion of STAU1 or 2 using shRNAs specific for each isoform increased perinuclear partitioning of *CEBPB* transcripts (Figs. 4E and S4B). High-resolution imaging revealed the presence of *CEBPB* mRNAs juxtaposed to CK2α foci after STAU1/2 silencing (Fig. 4F), similar to the situation in UPF1-depleted cells (Fig. 3A). This finding raises the intriguing possibility that STAU1/2 regulate *CEBPB* mRNA decay on or near CK2-containing endosomes. Live cell imaging

of fluorescently tagged CK2α and STAU1/2 reveals almost complete overlap between CK2α and STAU-positive foci (Fig. 4G), indicating that STAU1/2 are recruited to CK2-associated endosomes. Finally, ablation of either STAU isoform triggered senescence that was partly dependent on C/EBPβ (Fig. S4C). STAU silencing also induced pro-inflammatory SASP genes (Fig. S4D), although the increase was less than for UPF1 knockdown (Figs. 3 and S3). UPF1 and STAU1/2 therefore target *CEBPB* mRNA decay to CK2 signaling endosomes in cancer cells.

Identification of a STAU binding site (SBS) adjacent to the GRE region

A comparison of human and mouse *CEBPB* 3'UTRs shows that the 3' region encompassing the GRE displays highest conservation (Fig. S5A). An RNA secondary structure model (RNAFold) (Gruber et al., 2008) predicts a stem-loop feature formed by part of the GRE paired with a 5' adjacent sequence (Figs. 5A and S5A,B). A segment of this potentially double-stranded region is nearly identical in the two homologs and is similar to a known STAU binding site (SBS) in the *ARF1* 3'UTR (Kim et al., 2005) (Figs. S5C and 5A), suggesting it might function to recruit STAU proteins to the *CEBPB* 3'UTR. RNA-CLIP mapping in $3T3^{RAS}$-β^{UTR} cells using tiled PCR amplicons across the *Cebpb* 3'UTR showed a peak of Stau1 and Stau2 binding at a region spanning the GRE and putative SBS (Fig. 5B), indicating the presence of a functional SBS within this segment.

We generated deletion mutants in murine *Cebpb* lacking the SBS, SBS+GRE and GRE sequences (Fig. 5C). The 5' endpoint of the latter maintains the full SBS-like sequence and is denoted ΔGRE^{S} to distinguish it from the slightly longer ΔGRE (ARE) deletion described previously (Basu et al., 2011), which corresponds to mouse ΔGRE allele (see below). A subset of these mutants, together with $Cebpb^{UTR}$, were expressed in $3T3^{RAS}$ cells and nRIP assays were

performed to assess STAU binding. Stau2 associated with *Cebpb*^{UTR} transcripts but showed much less binding to *Cebpb*$^{\Delta SBS\text{-}GRE}$ and *Cebpb*$^{\Delta UTR}$ (Fig. 5C). Stau1 binding was less apparent but showed a similar pattern thoughout the constructs. Thus, Stau1/2 binding to the *Cebpb* 3'UTR is reduced when the SBS is deleted. When expressed in A549 cells, *Cebpb* transcripts lacking the SBS displayed more overlap with CK2α when compared to *Cebpb*^{UTR} (Fig. 5D). Moreover, when transfected together with HRAS^{G12V} in HEK 293T cells, *Cebpb*$^{\Delta UTR}$ and *Cebpb*$^{\Delta SBS}$ showed strongest phosphorylation on the C/EBPβ CK2 site, Ser222 (Fig. S5D). When a panel of these constructs was expressed in 3T3^{RAS} cells, p-Ser222 levels were increased in mutants lacking the SBS (Fig. 5E). All except *Cebpb*^{UTR} efficiently induced senescence (Fig. 5F) and caused decreased focus formation (Fig. S5E). The senescence phenotype was recapitulated in A549 cells expressing these constructs (Fig. S5F). Strikingly, only *Cebpb*$^{\Delta UTR}$ stimulated expression of SASP genes in 3T3^{RAS} cells (Fig. 5G). Thus, in transformed cells the SBS suppresses C/EBPβ phosphorylation by CK2, both the SBS and GRE motifs inhibit senescence, while another 3'UTR sequence appears to restrain C/EBPβ-induced SASP gene expression.

Senescence but not the SASP induced by oncogenic RAS in *p19*$^{Arf-/-}$;*Cebpb-GRE*$^{\Delta/\Delta}$ MEFS

To investigate the *in vivo* relevance of the UPA mechanism, we generated a mouse strain carrying a deletion of the *Cebpb* GRE region, which also removes part of the SBS (Fig. S6A). Homozygous mutant animals (*GRE*$^{\Delta/\Delta}$) were viable, fertile, and displayed no overt phenotypes. An aging study comparing *WT* and *GRE*$^{\Delta/\Delta}$ mice revealed no differences in longevity or susceptibility to disease (Fig. S6A).

To begin to address whether the *GRE*$^{\Delta/\Delta}$ genotype confers resistance to RAS-induced transformation, we crossed the mutant strain to mice lacking the *p19*^{Arf} tumor suppressor and

prepared MEFs of four genotypes: *WT*, $GRE^{\Delta/\Delta}$, $p19^{Arf-/-}$, and $p19^{Arf-/-};GRE^{\Delta/\Delta}$. As C/EBPβ UPA is abrogated in RIS cells but not in RAS-transformed tumor cells (Basu et al., 2018a) and $p19^{Arf}$ deficiency circumvents senescence to facilitate neoplastic transformation, we reasoned that *ΔGRE* phenotypes may be more apparent in cells lacking $p19^{Arf}$. RAS-induced phosphorylation on Ser222 was enhanced more ~1.7-fold in $p19^{Arf-/-};GRE^{\Delta/\Delta}$ MEFs compared to $p19^{Arf-/-}$ cells (Fig. 6A). $p19^{Arf-/-};GRE^{\Delta/\Delta}$ cells also formed fewer RAS-transformed foci (Fig. 6B). These effects were also seen in *WT* and $GRE^{\Delta/\Delta}$ MEFs depleted for $p19^{Arf}$ using RNAi (Fig. S6B).

$GRE^{\Delta/\Delta}$ MEFS without RAS displayed greater SA-βGal positivity than *WT* cells and thus senesce prematurely (Figs. 6C and S6C). Upon $HRAS^{G12V}$ expression, senescence of $GRE^{\Delta/\Delta}$ cells increased further and remained elevated compared to *WT* RIS cells. Whereas $p19^{Arf-/-}$ cells did not undergo RIS, $p19^{Arf-/-};GRE^{\Delta/\Delta}$ MEFs became senescent and displayed an enlarged, flattened morphology (Figs. 6C and S6C). Thus, the GRE deletion unleashes the RAS-induced pro-senescence functions of C/EBPβ in $p19^{Arf-/-}$ MEFs. $HRAS^{G12V}$ activated pro-inflammatory SASP genes equivalently in *WT* and $GRE^{\Delta/\Delta}$ MEFS (Fig. S6D), but little induction was seen in $p19^{Arf-/-}$ cells (Fig. 6D). Notably, $p19^{Arf-/-};GRE^{\Delta/\Delta}$ MEFs also failed to express the SASP despite becoming senescent. This phenotype is similar to that of $3T3^{RAS}$ cells over-expressing *CEBPB* mutants lacking the GRE and/or SBS elements (Figs. 5F,G) and provides further evidence that a separate 3'UTR sequence inhibits the transcriptional activity of C/EBPβ toward SASP genes. A notable exception is S100A9, which was strongly induced by RAS in $p19^{Arf-/-};GRE^{\Delta/\Delta}$ MEFs but not $p19^{Arf-/-}$ cells (Figs. 6D and S6E). S100A9 is a secreted Ca^{++} binding protein with pro-inflammatory properties that binds to TLR4 and activates the inflammasome (Place and Kanneganti, 2018). S100A9 induces senescence in bone marrow mesenchymal cells (Shi et al.,

2019) and thus could potentially act as an autocrine/paracrine RIS effector in *p19*$^{Arf-/-}$*;GRE*$^{\Delta/\Delta}$ cells.

Kras^{G12D}-driven lung tumors in _Cebpb-GRE_$^{\Delta/\Delta}$ mice show impeded progression to adenocarcinoma

To extend the above findings to an *in vivo* setting, we crossed *GRE*$^{\Delta}$ mice to the cancer prone strain, *KRas*^{LA2}, which develops lung tumors at high penetrance (Johnson et al., 2001). Pulmonary lesions in this model are predominantly benign adenomatous hyperplasias and alveolar adenomas, although some progress to malignant adenocarcinomas (ADCs). Groups of *KRas*^{LA2}/+ and *KRas*^{LA2}/+*;GRE*$^{\Delta/\Delta}$ mice were aged until accumulated pulmonary tumors or other lesions required euthanasia. There was no difference in survival between the two genotypes (Fig. 7A). Overall tumor burdens (sum of all tumor areas) showed a modest reduction in *GRE*$^{\Delta/\Delta}$ mice that was not significant (p=0.09) (Fig. 7B). However, histopathological evaluation of lesions showed differences in the most severe grade observed. ADCs were the most advanced tumors seen in 71.4% of *WT* mice compared to 14.3% in the *GRE*$^{\Delta/\Delta}$ cohort (p=0.0016; Fisher's exact test) (Fig. 7C). Using a supervised, AI-based algorithm (HALO image analysis software; Indica Labs) trained on H&E images to distinguish benign adenomas from atypical cells/ADCs, we quantitated areas corresponding to each tumor grade in each lung section (Fig. 7D). Although adenomas were similar between the two genotypes, areas of adenocarcinoma were nearly 4-fold greater in *WT* vs. *GRE*$^{\Delta/\Delta}$ animals (p=0.0244). This difference was not attributable to age at sacrifice, as there was no correlation between age and ADC burden in either genotype (Fig. S7A). Ki67 staining in ADC areas did not differ between the two genotypes (Fig. S7B), indicating that rare tumors that evade the *GRE*$^{\Delta/\Delta}$ blockade are able to achieve a high proliferate rate.

A characteristic feature of cancer cells is variability in nuclear size and shape. To determine if *WT* and $GRE^{\Delta/\Delta}$ tumors exhibit differences in anisokaryosis, selected regions of adenoma and ADC were analyzed for nuclear size heterogeneity using HALO AI. While distributions of nuclear size were similar in adenomas, $GRE^{\Delta/\Delta}$ ADC lesions contained significantly fewer karyomelagic cells compared to *WT* tumors ($p<0.0001$). These findings are consistent with $GRE^{\Delta/\Delta}$ cancers having a less malignant phenotype.

Discussion

UPA inhibits C/EBPβ activity in tumor cells through 3'UTR-mediated exclusion of *CEBPB* transcripts from the kinase-rich perinuclear region (Basu et al., 2011). We now identify perinuclear mRNA decay (PMD) as the mechanism for selectively eliminating *CEBPB* mRNAs from the nuclear-proximal compartment. We show that UPF1 and STAU, which are well documented mRNA decay proteins, play key roles in PMD. The *CEBPB* GRE sequence and an adjacent SBS motif form a composite element that recruits HuR and STAU1/2 to activate UPF1-dependent mRNA decay. PMD also requires SMG6 and SMG7, but not SMG5 or the UPF1 kinase, SMG1. These features distinguish PMD from NMD and other types of UPF1-dependent RNA degradation (Kim and Maquat, 2019). Although PMD involves STAU, it differs from SMD, which requires SMG1 (Cho et al., 2013). Thus, PMD can be considered a unique class of mRNA decay.

The subcellular location of PMD is essential to suppress C/EBPβ phosphorylation in tumor cells, as the C/EBPβ kinases CK2 and ERK are present on perinuclear signaling endosomes (Basu et al., 2018b). Localized *CEBPB* mRNA decay is specified by the perinuclear segregation of UPF1 and STAU, which are inversely correlated with *CEBPB* transcripts. Live cell imaging showed nearly complete overlap of STAU1 and STAU2 with CK2 puncta (Fig. 4G). This result indicates

that *CEBPB* mRNA decay is in fact highly localized to signaling endosomes, providing a compelling mechanism for increased phosphorylation on C/EBPβ Ser222 (CK2 site) when the SBS is deleted (Figs. 5E and S5D).

This idea is further supported by high resolution images showing that depletion of UPF1 or STAU1/2 caused *CEBPB* transcripts to colocalize with CK2 puncta (Figs. 3A and 4F). These observations suggest the existence of an active mRNA homing mechanism that is disclosed when PMD is disrupted. Since *CEBPB* transcripts lacking the 3'UTR also exhibit association with CK2, there could be an RNA localization determinant within the coding region. Alternatively, a signal within the nascent C/EBPβ protein might direct the attachment of *CEBPB* polysomes to CK2-containing endosomes. The proximity between *CEBPB* mRNAs and CK2 suggests an obligatory co-translational modification mechanism, whereby phosphorylation must occur during protein synthesis (Fig. S7C). This spatial coupling would explain why C/EBPβ translated outside the perinuclear domain remains in an unphosphorylated, low activity state. The default propensity of *CEBPB* mRNAs to localize near CK2 signaling endosomes underscores the importance of PMD in preventing C/EBPβ phosphorylation/activation to suppress senescence in tumor cells.

An unexpected finding of our study was that the pro-senescence and SASP-inducing activities of C/EBPβ are inhibited by distinct 3'UTR elements. This is clearly demonstrated by the different responses of tumor cells to expression of $Cebpb^{UTR}$ (neither senescence nor the SASP), ΔGRE and/or SBS (senescence only), or $Cebpb^{\Delta UTR}$ (senescence and the SASP). Further evidence comes from the senescence-prone but SASP-less phenotype of immortalized $GRE^{\Delta/\Delta}$ MEFs expressing oncogenic RAS. Hence, while the SBS/GRE region is required to inhibit senescence, deletion of this sequence does not lead to activation of SASP genes, implicating another 3'UTR sequence in suppressing the latter. This conclusion is reinforced by the fact that HuR depletion

induces senescence but only weakly activates the SASP (Fig. S1B), similar to deletion of its cognate GRE site. In contrast, UPF1 silencing activates C/EBPβ-dependent senescence and the SASP, indicating that mRNA decay is central to both inhibitory mechanisms. If so, it is likely that decay occurs in multiple subcompartments, since a generalized perinuclear decay mechanism is difficult to reconcile with two 3'UTR elements having distinct UPF1-dependent inhibitory functions. These considerations suggest an intriguing model whereby mRNA degradation is directed to discrete perinuclear kinase locations. In support of this idea, ERK and CK2 are tethered to different classes of signaling endosomes (Basu et al., 2018b), which might provide platforms to recruit distinct mRNA decay factors. Such organization could extend to other kinases as well. In this manner, multiple decay elements in the 3'UTR could independently suppress C/EBPβ phosphorylation at various sites. Validation of this hypothesis will require a more detailed understanding of the mechanism by which a distinct 3'UTR element inhibits C/EBPβ transcriptional activity toward SASP genes.

GRE$^{\Delta/\Delta}$ mice exhibited no obvious phenotypes, indicating that at least the GRE-dependent aspects of UPA are not essential for normal mouse development or physiology. However, in a *Kras*^{G12D}-driven model of lung carcinogenesis, the *ΔGRE* mutant suppressed development of malignant adenocarcinomas. These findings provide the first evidence that UPA regulation is manifested *in vivo*. Development of benign adenomatous lesions was unaffected, indicating that UPA becomes critical when tumors progress to the carcinoma stage. *Kras*^{LA2}-driven lung ADCs are characterized by elevated RAS pathway signaling, with increased p-ERK levels compared to adenomas (Feldser et al., 2010). High RAS pathway flux activates C/EBPβ, which would impede growth of adenocarcinomas without the constraint of UPA. Amplified RAS signaling also engages pro-senescence pathways such as Arf/p53 (Lin et al., 1998), creating selective pressure for loss of

tumor suppressor genes in malignant cancers (Feldser et al., 2010). We propose that such events, particularly loss of ARF, are linked to implementation of C/EBPβ UPA. This is supported by the observation that the *GRE*$^{\Delta/\Delta}$ genotype restores RAS-induced senescence in *p19*$^{Arf-/-}$ MEFs (Fig. 6). The UPA mechanism could extend to other tumor suppressor proteins, whose activities may be similarly held in check by 3'UTR regulation.

Acknowledgements

We thank Kristen Lynch for insightful comments, Eugene Valkov for suggesting the *Malat1* experiment and providing constructs, and Dominic Esposito for RAS vectors. This research was supported in part by the Intramural Research Program of the NIH, National Cancer Institute, Center for Cancer Research, and in part with Federal funds from the National Cancer Institute, National Institutes of Health, under Contract No. HHSN261200800001E. The content of this publication does not necessarily reflect the views or policies of the Department of Health and Human Services, nor does mention of trade names, commercial products, or organizations imply endorsement by the U.S. Government.

Methods

Cell lines

Mouse NIH 3T3 and 3T3^{Ras} fibroblasts were cultured in DMEM supplemented with 10% calf serum. Mouse embryonic fibroblasts (MEFs), human A549, PANC-1, SW-900, IMR-90, GP2 and HEK 293T cell lines were cultured in DMEM supplemented with 10% fetal bovine serum. All cell lines were cultured with 100 µg/mL primocyn, maintained at subconfluency and grown in a humidified incubator at 37 ºC with 5% CO_2. Cells infected with retroviral/lentiviral plasmids were

selected with 2 µg/mL puromycin for 2 days or 100 µg/mL hygromycin for 4 days or 800 µg/mL G418 for 7 days.

Animal studies

All animals were maintained in compliance with National Institutes of Health animal guidelines and experimental procedures were approved by the Animal Care and Use Committee, National Cancer Institute at Frederick. *p19*$^{Arf-/-}$ (*CdKn2a-Arf*) mice were obtained from the NCI-Frederick repository on a mixed background (B6.129). This strain was continuously backcrossed to C57Bl/6Ncr and maintained as homozygous stocks. *Cebpb-GRE*^{flox} mice were generated in house by injection of ES cells containing the targeted *GRE*^{flox} allele (*LoxP* sites flanking 102-nt mouse *Cebpb* GRE region; 3'UTR nucleotides 308-409) into C57BL/6Ncr mouse blastocysts. The germline GRE$^{\Delta}$ allele was generated by mating *GRE*^{flox} mice with *ACTB-Cre* mice (Lewandoski et al., 1997). GRE$^{\Delta}$ mice were backcrossed to *WT* C57BL/6Ncr animals and maintained as heterozygous stocks. *p19*$^{Arf-/-}$*;GRE*$^{\Delta/+}$ strain (C57BL/6Ncr) was obtained by continued intercrossing of *p19*$^{Arf-/-}$ *and GRE*$^{\Delta/+}$ mice and maintained by *p19*$^{Arf-/-}$*; GRE*$^{\Delta/+}$ crosses. *Kras*$^{G12D-LA2/+}$ mice (Johnson et al., 2001) were maintained by crossing to *WT* (129/SV). To obtain the *Kras*$^{LA2/+}$*;GRE*$^{\Delta/+}$ strain, *Kras*$^{LA2/+}$ (129/SV) and *GRE*$^{\Delta/+}$ (C57BL/6Ncr) mice were crossed. The mixed B6.129 background F1 progeny were bred (*Kras*$^{LA2/+}$*;GRE*$^{\Delta/+}$ X *Kras*$^{+/+}$*;GRE*$^{\Delta/+}$) to produce experimental animals. Mouse embryonic fibroblasts (MEFs) were prepared from embryonic day 13.5 (E13.5) embryos of the indicated genotypes.

Xenograft experiments

Six- to eight-week-old Balb/c athymic nude mice were randomly grouped. The mice were warmed with an incandescent lamp to induce vasodilation, placed in a commercial restraint device, and injected via the lateral tail vein with 1 x 10^6 A549 cells or derivatives suspended in 100 µl of phosphate buffer saline (PBS). Animals were euthanized 7 weeks post-injection using CO_2 inhalation. The entire lung and bronchi were harvested, lung nodules were counted and measured. The lungs were inflated using 10% Neutral Buffered Formalin (NBF) before placing into a container of the same fixative. To ensure proper fixation stability, after five days in fixative, the tissues were removed from 10% NBF and placed into 70% ethanol.

Plasmids

Oligonucleotides encoding short hairpin transcripts targeting mouse *Anxa1, Anxa2, Celf1, Dhx9, Fmr1, Fubp1, Fubp2, Fubp3, Hnrnpa2b1, Hnrnpd, Igf2bp1, Igf2bp2, Igf2bp3, Ilf2, Ilf3, Mapre1, Nono, Plec, Strbp* and *Upf1* (Table S1) were inserted between the BamHI and EcoRI sites of the knockdown vector pSirenRetroQ-puro (Clontech). The knockdown vectors for mouse *Cebpb* (Cebpb1 shRNA) and human *CEBPB* have been described (Sebastian and Johnson, 2009). The expression vectors pcDNA3.1(-)-β^{UTR}, pcDNA3.1(-)-$\beta^{\Delta UTR}$, pBabe-β^{UTR}, pBabe-$\beta^{\Delta UTR}$, and knockdown vector pSuperRetro-shElavl have been described previously (Basu et al., 2011). Lentiviral plasmids CMV51p-$HRAS^{G12V}$ (hygro) and control CMV13p (hygro) were obtained from Dr. Dominic Esposito (RAS Initiative, Frederick National Laboratory for Cancer Research). The triple helix sequence from mouse noncoding RNA *Malat1* (Wilusz et al., 2012) and its control scrambled sequence were inserted into the 3' end of pBabe-βUTR using synthetic oligos harboring PacI and SbfI restriction sites. The ΔSBS, ΔGRE^{S}, ΔSBS-GRE deletions were generated by replacing the sequence listed in Table S1 with a BamHI site. Briefly, two PCR products, containing

NheI/BamHI 5' fragment and BamHI/HindIII 3' fragment, were cloned into pcDNA3.1(-)-$\beta^{\Delta UTR}$ by three-way ligation. Each sequence was transferred from pcDNA to pBabe retroviral vector using EcoRI and SalI sites. A complete list of plasmids and sequences is included in Table S1.

Retroviral and lentiviral infections

Packaging GP2 cells (for retroviral plasmids) or HEK 293T cells (for lentiviral plasmids) were seeded at 3 x 10^6 cells per 100 mm culture dish for 24 h before transfection with 20 µg of the viral expression plasmid containing the insert of interest. Plasmids were co-transfected by calcium phosphate precipitation together with the following packaging and/or envelope plasmids: 4 µg of pVSVG (for retroviral plasmids) or 6 µg of pMD2.G, 10 µg of pMDL g/p RRE, 5 µg of pRSV-Rev (for lentiviral plasmids). Supernatants containing infectious viral particles were harvested at 24, 36 and 48 h post-transfection and filtered through 0.45 µm PVDF filters. Cells were cultured in 100 mm culture dishes for 24 h before infection with viral supernatants in the presence of 8 µg/mL polybrene.

Transient transfection

HEK 293T cells were transfected with 100 ng of pcDNA 3.1(-)-$HRAS^{G12V}$, 1 µg of pcDNA 3.1(-) empty vector or C/EBPβ deletion mutants in 100 mm dishes using X-tremeGENE HP (Roche) according to manufacturer's instructions. After transfection, cells were cultured for 48 hours before harvesting.

Protein lysates

For cytoplasmic and nuclear fractionation, cells were rinsed twice with ice-cold PBS, resuspended in hypotonic Buffer A (20 mM HEPES [pH 7.9], 1 mM EDTA, 10 mM NaCl, 1 mM DTT, 0.1% NP-40 substitute, 1X protease and phosphatase inhibitor sets) and incubated on ice for 10 min. Nuclei were pelleted by centrifugation for 10 min at 1,200 x g at 4 ºC. Supernatants (cytoplasmic extract) were frozen at -80 ºC. Nuclear pellets were rinsed with Buffer A (without NP-40) to remove residual cytoplasmic contaminants. Nuclear proteins were extracted by incubation of nuclei in hypertonic Buffer C (25 mM HEPES [pH 7.9], 0.2 mM EDTA, 700 mM NaCl, 0.2 mM DTT, 25% glycerol, 1X protease and phosphatase inhibitor sets) for 30 min at 1,300 rpm at 4 ºC. Nuclear debris was pelleted by centrifugation for 10 min at 12,000 x g at 4 ºC, and the supernatant (nuclear extract) was stored at -80 ºC. Chromatin fractionation was performed as described with minor modifications (Mendez and Stillman, 2000; Narita et al., 2006). Briefly, cells were rinsed twice with ice-cold PBS, resuspended in Buffer A* (10 mM HEPES [pH 7.9], 10 mM KCl, 1.5 mM $MgCl_2$, 340 mM sucrose, 10% glycerol, 0.1% NP-40, 1 mM DTT, 1X protease and phosphatase inhibitor sets) and incubated on ice for 10 min. Nuclei were pelleted by centrifugation for 5 min at 1,200 x g at 4 ºC. Obtained supernatant was labeled as cytoplasmic extract and frozen at -80 ºC. Nuclear pellets were rinsed with Buffer A* (without NP-40) to remove residual cytoplasmic contaminants. Nuclear pellet was incubated with Buffer B (3 mM EDTA, 0.2 mM EGTA, 1 mM DTT, 1X protease and phosphatase inhibitor sets) for 30 min at 1,300 rpm (thermomixer) at 4 ºC. Insoluble chromatin fraction was collected by centrifugation for 4 min at 1,300 x g at 4 ºC, and the supernatant was designated as nucleoplasmic extract and stored at -80 ºC. Insoluble chromatin fraction was gently rinsed three times with ice-cold Buffer B and collected by centrifugation for 4 min at 1,300 x g at 4 ºC. Chromatin-bound proteins were obtained by incubation of insoluble chromatin fraction with DNase I solution (0.1 U/µL DNase I, 10 mM Tris-

HCl pH 7.5, 2.5mM $MgCl_2$, 0.1 mM $CaCl_2$, 1X protease and phosphatase inhibitor sets) at 37 °C for 1 h. Soluble chromatin fraction was cleared by centrifugation at 16,000 × g, 10 min, 4 °C and supernatant was frozen at -80 ºC. For whole cell lysates, cells were rinsed twice with ice-cold PBS, harvested in RIPA buffer (10 mM Tris pH 7.4, 150 mM NaCl, 1 mM EDTA, 0.5% sodium deoxycholate, 0.1% SDS, 1% Triton-X, 1X protease and phosphatase inhibitors sets), kept on ice for 10 min, and centrifuged for 10 min at 12,000 x g at 4 ºC. Supernatant was stored at -80 ºC. Protein concentrations were determined by Bradford protein assay (Bio-Rad).

RNA affinity purification of GRE interacting proteins

The RNA pull-down method was modified from Butter et al. (2009). The GRE and GFP sequences were fused to the S1 aptamer tag, which was selected to have high affinity for streptavidin (Srisawat and Engelke, 2001). The GRE and GFP templates for *in vitro* transcription (TranscriptAid T7 High Yield Transcription Kit, ThermoFisher) were purified PCR products made with oligonucleotides containing the T7 RNA polymerase promoter sequence at the 5' end and the aptameric tag at the 3' end (Table S1). The RNA was purified using phenol/chloroform standard protocols and stored in RNase-free water at -80 ºC. The S1-tagged RNA was refolded by heating for 3 min at 95 ºC, cooling on ice for 2 min, adding the RNA buffer (10 mM Tris-HCl [pH 8.0], 150 mM NaCl, 1 mM $MgCl_2$, 0.1 mM EDTA) and incubating for 20 min at 20 ºC. The RNA was bound to RNase-free Dynabeads MyOne Streptavidin C1 (ThermoFisher) in RNA binding buffer (RBB, 50 mM Hepes·[pH 7.4], 150 mM NaCl, 0.5% NP-40 substitute, 10 mM $MgCl_2$) by incubation with gentle rotation for 30 min at 4 ºC, followed by three washes with RBB. Beads were incubated with 400 µg NIH 3T3 cytoplasmic extract (in Buffer A with NaCl concentration adjusted to 150 mM and prepared with RNase inhibitor), 40 U of RNase inhibitor (ThermoFisher),

and 20 µg of yeast tRNA (ThermoFisher) for 30 min at 4 ºC (final volume 100 µL). After three RBB washes with gentle rotation for 10 min each at 4 ºC, the RNA was competed from the beads with elution buffer (16 mM biotin, 50 mM Hepes [pH 7.4], 250 mM NaCl, 0.5% NP-40 substitute, 10 mM $MgCl_2$). Eluates were frozen at -80 ºC until used for immunoblotting or MS analysis.

Mass spectrometry (LC-MS/MS) to identify GRE interacting proteins

Coomassie stained gel bands were chopped to small pieces and destained using 50% CAN, 25 mM NH_4HCO_3 [pH 8.4]. After removal of organic solvent, the gel pieces were vacuum dried for 45 min. The dried gel pieces were rehydrated in 50 µL of trypsin (20 ng/ µL) resuspended in 25 mM NH_4HCO_3 and incubated on ice for 30 min. Excess trypsin was removed and replaced with 30 µL of 25 mM NH_4HCO_3 [pH 8.4]. The samples were incubated at 37 ºC for 16-18 hr. Peptides were extracted from the gel bands with 70% (v/v) CAN, 0.1% TFA. The extracted peptides were lyophilized, desalted using C18 columns (ThermoFisher) and reconstituted in 0.1% TFA. The peptides were analyzed using mass spectrometry as described below. The samples were subjected to nanoflow liquid chromatography on a 25 cm Acclaim PepMap C18 column (Easy nLC 1200, Thermo Scientific) coupled to high resolution tandem mass spectrometer (Q Exactive HF, ThermoFisher). MS precursor scans were performed at a resolution of 60,000 with an ion accumulation target set at $1e^6$, maximum IT at 120 ms, over a mass range of 380-1580 m/z. MS2 analysis was performed at a resolution of 15,000 with an ion accumulation target set at $2e^5$, maximum injection time at 50 ms, at an isolation with of 1.4 m/z over a scan range of 200 to 2000 m/z. Top 20 precursor ions were selected for fragmentation at a normalized collision energy of 27, charge state 1 and >8 were excluded with a 25 second dynamic exclusion. Acquired MS/MS spectra were searched against the mouse Uniprot protein database using SEQUEST and the

Percolator validator algorithms in Proteome Discoverer 2.2 (ThermoFisher). The precursor ion tolerance was set at 10 ppm and the fragment ions tolerance at 0.02 Da. Maximum 2 missed cleavage side were allowed, a minimum peptide length was set at 6 amino acids with methionine oxidation as dynamic modification. A false discovery rate of 0.01 was used for the decoy database search for peptide identification.

MS data analysis. The MS results identified 25,188 PSMs bound to GRE representing 1107 proteins, and 13,352 PSMs bound to GFP representing 763 proteins (the sum of PSM counts from three independent affinity purification experiments was used). Overall, there were 4616 identified proteins that bind to either GPF or GRE. Since the GRE and GFP pull down experiments were run independently, the null hypothesis is that there should be no preference for binding to one or the other. By determining the number of PSMs from a protein that bound to GRE and the total number that were bound to either GRE or GFP, a Binomial test was used to determine if the number of GRE-bound PSMs is significantly different from that expected by chance. This p-value was Bonferroni corrected and then used to calculate the false discovery rate (FDR). Using a threshold FDR of 0.1, all proteins whose ratio of GRE-bound PSMs to GFP-bound PSMs was at least 2.0 were selected. The 324 proteins that show a significant preference for binding to GRE were submitted to DAVID (2021 Release) (Sherman et al., 2022) for functional analyses.

Immunoblotting

Equal amounts of total proteins were separated on 4-15% SDS-PAGE (Bio-Rad) and blotted to PVDF membranes (Bio-Rad). Membranes were blocked for 1 h in TBS-T buffer (20 mM Tris [pH 7.6], 150 mM NaCl, 0.1% Tween-20) containing 5% nonfat milk and were then incubated with primary antibodies for 16-18 h at 4 ºC. Membranes were rinsed three times in TBS-T, incubated

for 1 h at 20 ºC with the appropriate secondary antibodies in 5% nonfat milk (in TBS-T), then rinsed three times in TBS-T before imaging using chemiluminescent ECL substrate (ThermoFisher). All antibodies are listed in Table S1.

Immunoprecipitation (IP)

400 µg of cytoplasmic extract (where noted, with 200 µg/mL RNase A treatment for 10 min at 20 ºC) or 200 µg nuclear proteins were incubated with primary antibodies with gentle rotation for 3 h at 4 ºC in IP buffer (20 mM Tris [pH 8.0], 137 mM NaCl, 10% glycerol and 1% NP-40 substitute, 1X protease and phosphatase sets). Dynabeads™ Protein G (ThermoFisher) were added to the samples and incubated with gentle rotation for 1 h at 4 ºC. Immunocomplexes were washed four times in IP wash buffer (20 mM Tris [pH 8.1]; 137 mM NaCl; 0.5% NP-40; 1 mM EDTA) and eluted in 2X Laemmli sample buffer (Bio-Rad) with β-mercaptoethanol for 10 min at 95 ºC. Eluted samples were analyzed by immunoblotting. In the case of STAU proteins, immunocomplexes were eluted in 2X Laemmli sample buffer (Bio-Rad) with β-mercaptoethanol for 30 min at 20 ºC and Protein A conjugated with HRP (MilliporeSigma) was used in lieu of secondary antibody (Lal et al., 2005). Antibodies are listed in Table S1.

Native RNA immunoprecipitation (nRIP)

400 µg of cytoplasmic extracts (in Buffer A with 150 mM NaCl, 1 mM $MgCl_2$ and prepared with 400 U/mL RNase inhibitor) were incubated with primary antibodies (Table S1) with gentle rotation for 3 h at 4 ºC in NT-2 buffer (50 mM Tris [pH 7.4], 150 mM NaCl, 1 mM $MgCl_2$, 0.05% NP-40 substitute, 400 U/mL RNase inhibitor, 1X protease and phosphatase sets). Dynabeads™ Protein G (ThermoFisher) were added to the samples and incubated with gentle rotation for 1 h at 4 ºC.

Immunocomplexes were washed four times in NT-2 buffer, processed for RNA extraction/purification, and analyzed by RT-qPCR with sequence-specific primers (Table S1). For confirmation of immunoprecipitated proteins, the same protocol was performed in parallel with a modification on the elution step. After washes, beads were eluted in 2X Laemmli sample buffer (Bio-Rad) with β-mercaptoethanol for 10 min at 95 ºC. Eluted samples were analyzed by immunoblotting.

Crosslinking RNA immunoprecipitation (CLIP)

The CLIP procedure was modified from Niranjanakumari et al. (2002) and Yoon and Gorospe (2016). For STAU1 CLIP, cells were rinsed twice in PBS and 0.7% formaldehyde (in PBS) was added directly to the dishes. Cells were incubated for 10 min at 20 ºC with rocking and the cross-linking reaction was quenched with 125 mM glycine for 5 min at 20 ºC. Cells were extensively washed with ice-cold PBS, resuspended in ice-cold NT-2 Buffer (50 mM Tris [pH 7.5], 150 mM NaCl, 1 mM $MgCl_2$, 0.05 % NP-40, 1X protease and phosphatase inhibitor sets) and kept for 10 min on ice. Lysates were treated with 200 U/mL MNase in the presence of 5 mM $CaCl_2$ for 5 min at 37 ºC to obtain RNA fragments. After incubation, 10 mM EGTA was added to inactivate MNase reaction. For STAU2 CLIP, cells were rinsed twice in PBS and 3.7% formaldehyde (in PBS) was added directly to the dishes. Cells were incubated for 10 min at 20 ºC with rocking and the cross-linking reaction was quenched with 125 mM glycine for 5 min at 20 ºC. Cells were extensively washed with ice-cold PBS, resuspended in ice-cold NT-2 Buffer (with 400 U/mL RNase inhibitor) and kept for 10 min on ice. 500 µL of lysates were sonicated to obtain RNA fragments (Bioruptor, 15 sec ON/45 sec OFF for 10 min at 4 ºC on LOW settings). For both STAU1/2 CLIP, lysates were cleared by centrifugation for 5 min at 12,000 x g at 4 ºC. Lysates (400 µg) were incubated

for 16 h at 4 ºC with primary antibodies in NT-2 Buffer (with 400 U/mL RNase inhibitor). Dynabeads™ Protein G (ThermoFisher) were added to the samples and incubated with gentle rotation for 2 h at 4 ºC. Immunocomplexes were washed four times with NP-40 Buffer (20 mM Tris [pH 7.5], 100 mM KCl, 5 mM $MgCl_2$, 0.5 % NP-40) and processed for RNA extraction/purification with GeneJet RNA purification kit (ThermoFisher) with the addition of Proteinase K treatment, according to the manufacturer's protocol. Same volume of purified RNA samples was analyzed by RT-qPCR with sequence-specific primers (Table S1).

Electrophoretic mobility shift assay (EMSA)

Nuclear extracts were incubated with double-stranded oligonucleotide probe containing a consensus C/EBP binding site sequence labeled with [γ-^{32}P]ATP as previously described (Lee et al., 2010).

Quantitative real-time PCR

Total RNA was extracted and purified using QIAshredder (Qiagen) and GeneJet RNA purification kit (ThermoFisher) and reverse transcribed by using Maxima first strand cDNA synthesis kit for RT-qPCR with dsDNase (ThermoFisher) according to the manufacturers' protocols. Relative gene expression was measured by quantitative PCR using SsoAdvanced SYBR Green Supermix (Bio-Rad) and mouse or human gene-specific primers (listed in Table S1). *Ppia/PPIA* or *B2m/B2M* were used as normalization reference genes.

RNA FISH and immunofluorescence (IF) staining

For RNA FISH, Quanti-Gene ViewRNA ISH Cell Assay (ThermoFisher) was used according to the manufacturer's protocol with the following modifications. Cells were plated at 1-2 x 10^4 cells per chamber on µ-slides VI0.4 (Ibidi). After 1-2 days, cells were rinsed in ice-cold Cytoskeleton Buffer (CB; 10 mM MES pH 6.1, 150 mM NaCl, 5 mM $MgCl_2$, 5 mM EGTA, and 5 mM glucose) (Scheffler et al., 2014), permeabilized and fixed in ice-cold pre-fixative mix in CB (4% paraformaldehyde, 0.01% glutaraldehyde, 0.05% saponin) (Whelan and Bell, 2015) for 10 min at 4 ºC. Cells were then incubated with ice-cold fixative mix in CB (4% paraformaldehyde, 0.01% glutaraldehyde) for 2 h at 4 ºC. To better preserve localization of mRNA and proteins, cells were treated with SHIELD mix (SHIELD epoxy/SHIELD OFF buffer, 3:1 v/v) (Life Canvas Technology; Table S1) for 30 min at 37 ºC (Park et al., 2019). Cells were rinsed with CB twice and quenched with 50 mM NH_4Cl (in CB) for 5 min at 20 ºC. After FISH hybridization steps, cells were rinsed in PBS-S (0.05% Saponin, in PBS) and blocked with 5% albumin in PBS-S for 1 h at 20 ºC. Cells were then incubated with the indicated primary antibodies (Table S1) for 16-18 h at 4 ºC in 5% albumin in PBS-S. Cells were rinsed three times for 5 min at 20 ºC with PBS-S and incubated for 1 h at 20 ºC with AlexaFluor-conjugated secondary antibodies (Table S1) in 5% albumin in PBS-S. Cells were rinsed twice with PBS-S, co-stained with 0.1 mg/mL DAPI (in PBS) for 2 min at 20 ºC, and then rinsed three times with PBS. Slides were kept in PBS at 4 ºC for 1-3 days until imaging. Images were acquired using either a Zeiss LSM 780 or 880 confocal microscopes or a Zeiss LSM 880 Airyscan super-resolution microscope. Images were processed and analyzed using Zen black and Zen blue software (Zeiss).

mRNA quantification and image analysis

To quantify mRNA distribution in different areas of the cell, Imaris software version 9.8 (Bitplane, Belfast, UK) was used to fit mRNA signals to the spots module and protein signals to the surface module. The identified surfaces and spots were combined in the cells module to further elucidate the specific numbers of mRNA spots within a defined region of the cell. One spots module, three surface modules, and two cell modules were used to conduct the analysis. The mRNA signals were defined setting a defined size for the spot of 0.400 µm in XY and using a manual quality threshold value according to visual inspection of the image. There were multiple surfaces defined nuclei, kinase region, and cell boundaries. Nuclei were defined using the surface module and DAPI staining to identify individual nuclei. The protein signal from immunofluorescent staining of the CK2 kinase was used to define the kinase region using a manual threshold of high intensity signals and smoothing to find a defined region for CK2. The cell boundaries were determined by both oversaturating the kinase signal and using a DIC image of the cells. Two cell modules were built. Cell module one identified the cell boundary, nuclei, and mRNA spots. Cell module one was used to find mRNA spots in the cytoplasm and total mRNA spots within the entire cell. Cell module two identified the kinase region, nuclei, and mRNA spots. Cell module 2 was used to define mRNA spots in the kinase region. Number of *CEBPB* mRNA molecules per cell and % of *CEBPB* mRNA overlapping the kinase region per cell were calculated.

Live cell imaging

Cells were transduced with lentiviral supernatants of plasmids expressing fluorescently tagged proteins. After selection with the appropriate marker, cells were plated at 2 x 10^4 cells per chamber on µ-slides VI0.4 (Ibidi). The cells were observed with confocal microscopy the following day.

mRNA decay assay

mRNA decay rates were determine using 5-ethynyluridine (EU) labeled mRNA chase assay. A549 cells were plated at 10^5 cells/well in 6-well dishes. After 24 h, 0.1 mM EU was added to the media for 16 h. After incubation, cells were either harvested (time 0) or media was replaced without EU and the cells were cultured for the indicated time points before RNA harvesting to allow degradation of the labeled RNA (chase). The isolated EU-labeled RNA was used with the Click-iT Nascent RNA Capture Kit (ThermoFisher) according to the manufacturer's instructions.

Proximity ligation assay (PLA)

A549 cells were plated at 4 x 10^4 cells per chamber on µ-slides VI0.4 (Ibidi). The next day, cells were rinsed in ice-cold PBS and fixed with methanol for 15 min at -20 ºC, permeabilized with 0.05% Saponin in PBS for 5 min at 20 ºC and rinsed three times with PBS. After fixation, Duolink® in situ detection system (MilliporeSigma) was used according to the manufacturer's instructions (volumes were adjusted accordingly for µ-slides). Images were acquired using a Zeiss LSM 780 confocal microscope.

Colony forming assays

Cells were plated at 2000 cells per 100 mm culture dish. After 10-14 days in culture, colonies were fixed in 4% formaldehyde in PBS for 10 min, stained with 0.1% crystal violet for 30 min and counted.

Focus formation assays

Cells were plated at 1000 cells per 100 mm culture dish with 1.5 x 10^5 untransformed NIH 3T3 or *p19*$^{Arf-/-}$ MEFs (lawn). After 10-14 days, cells were fixed in 4% formaldehyde in PBS for 10 min, stained with 0.1% crystal violet for 30 min and foci were counted.

Senescence-associated β-Galactosidase (SA-βGal) assays

Cells were plated at 2.5 x 10^4 cells per well in 6-well plates. After 2-3 days, cells were stained using a senescence detection kit (MilliporeSigma) with modifications of the manufacturer's instructions. For mouse cell lines, the pH of the staining solution mix was lowered by adding 1.54 µL of 2 M HCl per 1 mL.

Immunohistochemical (IHC) staining

For Ki67 IHC staining, slides generated from paraffin blocks (5 µm sections) were dewaxed using xylene and then hydrated using a series of graded ethyl alcohols. Slides were stained with Hematoxylin and Eosin-Y (H&E) following standard protocols using the Sakura® Tissue-Tek® Prisma™ automated stainer. A regressive staining method was used. This method intentionally overstains tissues and then uses a differentiation step (Clarifier/Bluing reagents) to remove excess stain. After staining was completed, the slides were coverslipped using the Sakura® Tissue-Tek™Glass® automatic coverslipper, dried and were ready for review. IHC staining was performed on LeicaBiosystems' BondRX autostainer with the following conditions: Epitope Retrieval 1 (Citrate) for 20 min, Ki67 (Cell Signaling Technology #12202, 1:200 for 30 min), and the Bond Polymer Refine Detection Kit (LeicaBiosystems #DS9800, with omission of the PostPrimary Reagent). Rabbit monoclonal IgG XP® Isotype Control (Cell Signaling Technology) was used in place of Ki67 for the negative control. Slides were removed from the Bond autostainer,

dehydrated through ethyl alcohols, cleared with xylenes, and coverslipped. H&E and IHC slides were scanned at 20X using an Aperio AT2 scanner (Leica Biosystems, Buffalo Grove, IL) into whole slide digital images.

Image analysis

All image analysis was performed using HALO imaging analysis software (v3.3.2541.300; Indica Labs, Corrales, NM), and image annotations were performed in a blinded fashion. The lung sections were annotated with HALO manual annotation tools. Nonspecific regions such as esophagus, thymus, and trachea were excluded from analysis. Areas of artifact such as folds and tears were also omitted from analysis. The HALO random forest tissue classifier was used to automatically differentiate neoplastic cells from normal lung parenchyma to determine total tumor burdens. Ki67 image analysis was performed using cytonuclear algorithm in HALO version 3.3 to determine percentage of positive cells. HALO MiniNet AI tissue classifier was used to automatically differentiate tumor cells from normal lung parenchyma and to differentiate benign adenomas form malignant adenocarcinomas. The size of nuclei was measured from Ki67 IHC stained slides. Multiple nodules (adenomas and adenocarcinomas) were selected in two different layers. HALO Nuclei Seg (plugin) classifier was used to segment nuclei.

Histological examination

In the *Kras*^{LA2} model, expanding and replacing pulmonary parenchyma are multifocal, variably-sized, up to 7 mm diameter, well-demarcated, unencapsulated neoplastic foci composed of cuboidal to columnar epithelial cells arranged in either packets, solid sheets, and glands or forming papillary structures, supported by a fine fibrovascular stroma. Neoplastic cells in adenomatous

nodules have variably-distinct cell borders, moderate amounts of eosinophilic cytoplasm, and round to oval nuclei with finely-stippled chromatin, and indistinct nucleoli. The mitotic rate is less than 1 per 20 high-power field (HPF). Multifocally, within one or more nodules, neoplastic cells forming adenocarcinomas display anisocytosis, which arranges in disorganized glands or solid sheets. Neoplastic cells have either scant to moderate amount of eosinophilic to amphophilic cytoplasm or have clear cytoplasm. Nuclei are moderately pleomorphic with fine to coarse chromatin and have prominent nucleoli. Mitotic rate is 0 to 2 per 20 HPF. Within the adjacent parenchyma, multifocally alveolar spaces often contain alveolar macrophages.

Statistical analyses

Quantitative data are presented as means ± standard deviation with the number of measurements ("n") indicated in the figure legends, representing biological replicates in cell culture experiments and the number of mice in animal studies. Statistical analysis was performed in GraphPad Prism using Student's t test function, unless otherwise indicated in the figure legends. P-values less than 0.05 were considered significant.

REFERENCES

Acosta, J.C., Banito, A., Wuestefeld, T., Georgilis, A., Janich, P., Morton, J.P., Athineos, D., Kang, T.W., Lasitschka, F., Andrulis, M.*, et al.* (2013). A complex secretory program orchestrated by the inflammasome controls paracrine senescence. Nat Cell Biol *15*, 978-990.

Acosta, J.C., O'Loghlen, A., Banito, A., Guijarro, M.V., Augert, A., Raguz, S., Fumagalli, M., Da Costa, M., Brown, C., Popov, N.*, et al.* (2008). Chemokine signaling via the CXCR2 receptor reinforces senescence. Cell *133*, 1006-1018.

Basu, S.K., Gonit, M., Salotti, J., Chen, J., Bhat, A., Gorospe, M., Viollet, B., Claffey, K.P., and Johnson, P.F. (2018a). A RAS-CaMKKbeta-AMPKalpha2 pathway promotes senescence by licensing post-translational activation of C/EBPbeta through a novel 3'UTR mechanism. Oncogene *37*, 3528-3548.

Basu, S.K., Lee, S., Salotti, J., Basu, S., Sakchaisri, K., Xiao, Z., Walia, V., Westlake, C.J., Morrison, D.K., and Johnson, P.F. (2018b). Oncogenic RAS-Induced Perinuclear Signaling Complexes Requiring KSR1 Regulate Signal Transmission to Downstream Targets. Cancer Research *78*, 891-908.

Basu, S.K., Malik, R., Huggins, C.J., Lee, S., Sebastian, T., Sakchaisri, K., Quinones, O.A., Alvord, W.G., and Johnson, P.F. (2011). 3'UTR elements inhibit Ras-induced C/EBPbeta post-translational activation and senescence in tumour cells. EMBO J. *30*, 3714-3728.

Braig, M., and Schmitt, C.A. (2006). Oncogene-induced senescence: Putting the brakes on tumor development. Cancer Research *66*, 2881-2884.

Butter, F., Scheibe, M., Morl, M., and Mann, M. (2009). Unbiased RNA-protein interaction screen by quantitative proteomics. Proc. Natl. Acad. Sci. USA *106*, 10626-10631.

Cho, H., Han, S., Park, O.H., and Kim, Y.K. (2013). SMG1 regulates adipogenesis via targeting of staufen1-mediated mRNA decay. Biochim Biophys Acta *1829*, 1276-1287.

Coppe, J.-P., Desprez, P.-Y., Krtolica, A., and Campisi, J. (2010). The Senescence-Associated Secretory Phenotype: The Dark Side of Tumor Suppression. Annual Review of Pathology: Mechanisms of Disease *5*, 99-118.

Feldser, D.M., Kostova, K.K., Winslow, M.M., Taylor, S.E., Cashman, C., Whittaker, C.A., Sanchez-Rivera, F.J., Resnick, R., Bronson, R., Hemann, M.T., and Jacks, T. (2010). Stage-specific sensitivity to p53 restoration during lung cancer progression. Nature *468*, 572-575.

Flury, V., Restuccia, U., Bachi, A., and Muhlemann, O. (2014). Characterization of phosphorylation- and RNA-dependent UPF1 interactors by quantitative proteomics. Journal of proteome research *13*, 3038-3053.

Gantt, K., Cherry, J., Tenney, R., Karschner, V., and Pekala, P.H. (2005). An early event in adipogenesis, the nuclear selection of the CCAAT enhancer-binding protein {beta} (C/EBP{beta}) mRNA by HuR and its translocation to the cytosol. J. Biol. Chem. *280*, 24768-24774.

Gruber, A.R., Lorenz, R., Bernhart, S.H., Neubock, R., and Hofacker, I.L. (2008). The Vienna RNA websuite. Nucleic Acids Res. *36*, W70-74.

He, S., and Sharpless, N.E. (2017). Senescence in Health and Disease. Cell *169*, 1000-1011.

Herranz, N., and Gil, J. (2018). Mechanisms and functions of cellular senescence. J. Clin. Invest. *128*, 1238-1246.

Hoare, M., Ito, Y., Kang, T.W., Weekes, M.P., Matheson, N.J., Patten, D.A., Shetty, S., Parry, A.J., Menon, S., Salama, R.*, et al.* (2016). NOTCH1 mediates a switch between two distinct secretomes during senescence. Nat Cell Biol *18*, 979-992.

Huggins, C.J., Malik, R., Lee, S., Salotti, J., Thomas, S., Martin, N., Quinones, O.A., Alvord, W.G., Olanich, M.E., Keller, J.R., and Johnson, P.F. (2013). C/EBPgamma suppresses senescence and inflammatory gene expression by heterodimerizing with C/EBPbeta. Mol. Cell. Biol. *33*, 3242-3258.

Johnson, L., Mercer, K., Greenbaum, D., Bronson, R.T., Crowley, D., Tuveson, D.A., and Jacks, T. (2001). Somatic activation of the K-ras oncogene causes early onset lung cancer in mice. Nature *410*, 1111-1116.

Kang, T.W., Yevsa, T., Woller, N., Hoenicke, L., Wuestefeld, T., Dauch, D., Hohmeyer, A., Gereke, M., Rudalska, R., Potapova, A.*, et al.* (2011). Senescence surveillance of pre-malignant hepatocytes limits liver cancer development. Nature *479*, 547-551.

Kim, Y.K., Furic, L., Desgroseillers, L., and Maquat, L.E. (2005). Mammalian Staufen1 recruits Upf1 to specific mRNA 3'UTRs so as to elicit mRNA decay. Cell *120*, 195-208.

Kim, Y.K., and Maquat, L.E. (2019). UPFront and center in RNA decay: UPF1 in nonsense-mediated mRNA decay and beyond. RNA *25*, 407-422.

Kuilman, T., Michaloglou, C., Vredeveld, L.C., Douma, S., van Doorn, R., Desmet, C.J., Aarden, L.A., Mooi, W.J., and Peeper, D.S. (2008). Oncogene-induced senescence relayed by an interleukin-dependent inflammatory network. Cell *133*, 1019-1031.

Kurosaki, T., and Maquat, L.E. (2016). Nonsense-mediated mRNA decay in humans at a glance. J. Cell Sci. *129*, 461-467.

Lal, A., Haynes, S.R., and Gorospe, M. (2005). Clean Western blot signals from immunoprecipitated samples. Mol Cell Probes *19*, 385-388.

Lebedeva, S., Jens, M., Theil, K., Schwanhausser, B., Selbach, M., Landthaler, M., and Rajewsky, N. (2011). Transcriptome-wide analysis of regulatory interactions of the RNA-binding protein HuR. Mol Cell *43*, 340-352.

Lee, S., Shuman, J.D., Guszczynski, T., Sakchaisri, K., Sebastian, T., Copeland, T.D., Miller, M., Cohen, M.S., Taunton, J., Smart, R.C.*, et al.* (2010). RSK-mediated phosphorylation in the C/EBP{beta} leucine zipper regulates DNA binding, dimerization, and growth arrest activity. Mol. Cell. Biol. *30*, 2621-2635.

Lewandoski, M., Meyers, E.N., and Martin, G.R. (1997). Analysis of Fgf8 gene function in vertebrate development. Cold Spring Harb Symp Quant Biol *62*, 159-168.

Li, J.H., Liu, S., Zhou, H., Qu, L.H., and Yang, J.H. (2014). starBase v2.0: decoding miRNA-ceRNA, miRNA-ncRNA and protein-RNA interaction networks from large-scale CLIP-Seq data. Nucleic Acids Res. *42*, D92-97.

Lin, A.W., Barradas, M., Stone, J.C., van Aelst, L., Serrano, M., and Lowe, S.W. (1998). Premature senescence involving p53 and p16 is activated in response to constitutive MEK/MAPK mitogenic signaling. Genes Dev. *12*, 3008-3019.

Lopes-Paciencia, S., Saint-Germain, E., Rowell, M.C., Ruiz, A.F., Kalegari, P., and Ferbeyre, G. (2019). The senescence-associated secretory phenotype and its regulation. Cytokine *117*, 15-22.

Lopez de Silanes, I., Lal, A., and Gorospe, M. (2005). HuR: post-transcriptional paths to malignancy. RNA Biol *2*, 11-13.

Luo, J., Emanuele, M.J., Li, D., Creighton, C.J., Schlabach, M.R., Westbrook, T.F., Wong, K.K., and Elledge, S.J. (2009). A genome-wide RNAi screen identifies multiple synthetic lethal interactions with the Ras oncogene. Cell *137*, 835-848.

Mendez, J., and Stillman, B. (2000). Chromatin association of human origin recognition complex, cdc6, and minichromosome maintenance proteins during the cell cycle: assembly of prereplication complexes in late mitosis. Mol. Cell. Biol. *20*, 8602-8612.

Narita, M., Narita, M., Krizhanovsky, V., Nunez, S., Chicas, A., Hearn, S.A., Myers, M.P., and Lowe, S.W. (2006). A novel role for high-mobility group a proteins in cellular senescence and heterochromatin formation. Cell *126*, 503-514.

Niranjanakumari, S., Lasda, E., Brazas, R., and Garcia-Blanco, M.A. (2002). Reversible cross-linking combined with immunoprecipitation to study RNA-protein interactions in vivo. Methods *26*, 182-190.

Park, E., and Maquat, L.E. (2013). Staufen-mediated mRNA decay. Wiley interdisciplinary reviews. RNA *4*, 423-435.

Park, Y.-G., Sohn, C.H., Chen, R., McCue, M., Yun, D.H., Drummond, G.T., Ku, T., Evans, N.B., Oak, H.C., Trieu, W.*, et al.* (2019). Protection of tissue physicochemical properties using polyfunctional crosslinkers. Nature Biotechnology *37*, 73-83.

Place, D.E., and Kanneganti, T.D. (2018). Recent advances in inflammasome biology. Curr Opin Immunol *50*, 32-38.

Salotti, J., and Johnson, P.F. (2019). Regulation of senescence and the SASP by the transcription factor C/EBPbeta. Exp Gerontol *128*, 110752.

Scheffler, J.M., Schiefermeier, N., and Huber, L.A. (2014). Mild fixation and permeabilization protocol for preserving structures of endosomes, focal adhesions, and actin filaments during immunofluorescence analysis. Methods Enzymol *535*, 93-102.

Sebastian, T., and Johnson, P.F. (2009). RasV12-mediated down-regulation of CCAAT/Enhancer Binding Protein {beta} in immortalized fibroblasts requires loss of p19Arf and facilitates bypass of oncogene-induced senescence. Cancer Research *69*, 2588-2598.

Sebastian, T., Malik, R., Thomas, S., Sage, J., and Johnson, P.F. (2005). C/EBPbeta cooperates with RB:E2F to implement Ras(V12)-induced cellular senescence. EMBO J. *24*, 3301-3312.

Sherman, B.T., Hao, M., Qiu, J., Jiao, X., Baseler, M.W., Lane, H.C., Imamichi, T., and Chang, W. (2022). DAVID: a web server for functional enrichment analysis and functional annotation of gene lists (2021 update). Nucleic Acids Res.

Shi, L., Zhao, Y., Fei, C., Guo, J., Jia, Y., Wu, D., Wu, L., and Chang, C. (2019). Cellular senescence induced by S100A9 in mesenchymal stromal cells through NLRP3 inflammasome activation. Aging (Albany NY) *11*, 9626-9642.

Srisawat, C., and Engelke, D.R. (2001). Streptavidin aptamers: affinity tags for the study of RNAs and ribonucleoproteins. RNA *7*, 632-641.

Whelan, D.R., and Bell, T.D. (2015). Image artifacts in single molecule localization microscopy: why optimization of sample preparation protocols matters. Scientific reports *5*, 7924.

Wilusz, J.E., JnBaptiste, C.K., Lu, L.Y., Kuhn, C.D., Joshua-Tor, L., and Sharp, P.A. (2012). A triple helix stabilizes the 3' ends of long noncoding RNAs that lack poly(A) tails. Genes Dev. *26*, 2392-2407.

Yoon, J.H., and Gorospe, M. (2016). Cross-Linking Immunoprecipitation and qPCR (CLIP-qPCR) Analysis to Map Interactions Between Long Noncoding RNAs and RNA-Binding Proteins. Methods Mol Biol *1402*, 11-17.

Figure legends

Figure 1. The *Cebpb* 3'UTR GRE motif associates with mRNA decay factor Upf1.

(**A)** Model for binding of HuR and other proteins to the *Cebpb* GRE to establish 3'UTR inhibition (UPA). **(B)** Coomassie stained gel of proteins binding to the GRE RNA or a control GFP RNA. **(C)** Volcano plot of proteins displaying positive or negative enrichment for GRE binding, as determined by mass spectrometry. GRE/GFP peptide count ratios are the sum of three independent affinity purification experiments. A threshold of $\log_2$ GRE:GFP ratio ≥ 1; $-\log_{10}$ FDR ≥ 1 was used to identify 324 GRE-interacting proteins. Forty-four proteins had p-values $< 10^{-17}$ and were plotted as equal to 10^{-17} for graphing purposes only. **(D)** Gene ontology analysis of proteins preferentially binding to the GRE. GRE-enriched proteins were analyzed for associations with pathways/biological processes using DAVID (Sherman et al., 2022). GO terms for the 20 highest ranking biological processes are shown, ranked by p-value. **(E)** Upf1 was ablated in $3T3^{RAS}$ cells overexpressing $Cebpb^{UTR}$ (βUTR) or depleted for C/EBPβ (shβ), and expression of proinflammatory SASP mRNAs was measured by RT-qPCR. **(F)** Immunoblots confirming binding of HuR and Upf1 to the GRE RNA. Quantitation of binding enrichment (average of 5 experiments) is shown below. **(G)** Association of HuR and Upf1 with *Cebpb* transcripts in NIH 3T3 cells. nRIP assays from 3 independent assays are shown. Bottom: immunoblots showing IP of HuR and Upf1. **(H)** HuR and Upf1 associate in an RNA-dependent manner. IPs were performed using NIH 3T3 cell lysates in the absence or presence of 200 µg/mL RNase A.

Figure 2. UPF1, SMG6 and SMG7 direct perinuclear decay of *CEBPB* transcripts.

(A) UPF1 knockdown in A549 lung adenocarcinoma cells increases the perinuclear abundance of *CEBPB* transcripts. *CEBPB* mRNA was detected using single molecule RNA FISH. **(B)** Live cell imaging shows perinuclear localization of eCFP-tagged UPF1 and mCherry-tagged CK2α in A549 cells. **(C)** Overlap of perinuclear CK2α and *CEBPB* mRNA increases after UPF1 silencing in A549 cells. A perinuclear CK2α domain was defined by fluorescence thresholds, and the number of *CEBPB* mRNA signals within this domain was determined for each cell (85 cells were analyzed for shCtrl and 26 cells for shUPF1). **(D)** UPF1 and HuR depletion increases total *CEBPB* mRNA levels in A549 cells. mRNA levels were determined by RT-qPCR analysis of RNA samples from bulk cell populations, normalized to *PPIA* mRNA. **(E)** *CEBPB* mRNA is stabilized by depletion

of UPF1 or HuR. Decay rates were measured by EU pulse-chase labeling, followed by RT-qPCR analysis of EU-containing *CEBPB* transcripts, normalized to *PPIA* mRNA. **(F, G)** Silencing of SMG6 (**F**) or SMG7 (**G)** disrupts peripheral partitioning of *CEBPB* transcripts in A549 cells.

Figure 3. UPF1 depletion in tumor cells stimulates C/EBPβ activity and phosphorylation by CK2α.

(A) High resolution imaging reveals close apposition of *CEBPB* mRNAs and CK2α foci in the perinuclear cytoplasm of tumor cells depleted for UPF1. **(B)** Proximity ligation assay (PLA) demonstrates increased juxtaposition of C/EBPβ and CK2α in A549 cells upon UPF1 depletion. Right panel: PLA signal quantification, expressed as PLA puncta per cell (55 cells were analyzed for shCtrl and 21 cells for shUPF1). **(C)** Upf1 knockdown increases phosphorylation on C/EBPβ Ser222 (CK2 site). The experiment was performed using chromatin bound proteins from $3T3^{RAS}$-β^{UTR} cells to enrich for C/EBPβ. Samples were equalized for total C/EBPβ and then analyzed by immunoblotting using a p-Ser222 phospho-specific antibody. **(D)** Upf1 silencing stimulates C/EBPβ DNA-binding activity. The experiment was performed in $3T3^{RAS}$-β^{UTR} cells; nuclear extracts were analyzed by EMSA. The indicated EMSA bands were quantitated and normalized to C/EBPβ protein levels (ratios shown below). **(E-G)** UPF1 was ablated in A549 cells with or without *CEBPB* knockdown (shβ). Cell proliferation was analyzed in colony assays (n = 2) **(E)**, SA-βGal staining was used to analyze senescence (n $\geq$ 400 cells) **(F)**, and expression of SASP genes was determined using RT-qPCR (**G**). **(H)** 10^6 control or UPF1-depleted A549 cells were intravenously injected into nude mice. After seven weeks, lung nodules were counted (n = 14 animals per group). **(I, J)** Insertion of the *Malat1* stability element at the 3' end of the *Cebpb* mRNA disrupts peripheral localization of the transcripts and abrogates the inhibitory effect of the 3'UTR. **(I)** Mouse *Cebpb* retroviral constructs containing the *Malat1* triple helical element or a scrambled version inserted at the 3' end (top diagram) were used to infect A549 cells. $Cebpb^{UTR}$ (βUTR) and $Cebpb^{\Delta UTR}$ (ΔUTR) were included as controls. RNA FISH was performed using a *Cebpb* probe specific for the mouse gene. **(J)** SA-βGal staining was used to analyze senescence (n $\geq$ 400 cells).

Figure 4. STAU1 and STAU2 regulate *CEBPB* PMD in tumor cells.

(A) Stau1 and Stau2 are enriched in the GRE-bound fraction. Samples described in Fig. 1F were analyzed by immunoblots probed for Stau1 or Stau2. **(B)** Stau1/2 associate with *Cebpb* transcripts in NIH 3T3 cells. nRIP pull-downs were performed using Stau1 and Stau2 antibodies and analyzed by RT-qPCR to assess *Cebpb* mRNA enrichment. Bottom: immunoblots showing IP of Stau1 and Stau2. **(C, D)** STAU1 and STAU2 localize to the perinuclear region in A549 cells where they partially overlap with UPF1. **(C)** Live cell imaging of fluorescently tagged fusion proteins. **(D)** Immunofluorescence combined with *CEBPB* RNA FISH**. (E, F)** Depletion of STAU proteins disrupts perinuclear exclusion of *CEBPB* mRNAs (**E**) and increases mRNA overlap with CK2α (**F**). High resolution imaging reveals close apposition of *CEBPB* mRNAs and CK2α in the perinuclear cytoplasm of tumor cells upon depletion of STAU1 or STAU2. **(G)** Live cell imaging showing overlap of STAU1 and STAU2 with CK2α.

Figure 5. Stau1/2 bind to a putative SBS in the *Cebpb* 3'UTR that is required to suppress C/EBPβ phosphorylation by CK2.

(A) An RNA secondary structure model (RNAFold) of the murine *Cebpb* 3'UTR predicts a stem-loop feature formed by part of the GU-rich sequence (red) paired with a 5' adjacent sequence containing a putative SBS (blue). **(B)** CLIP mapping localizes Stau1 and 2 binding to the GRE region in $3T3^{RAS}$-β^{UTR} cells. Top, positions of PCR amplicons used for CLIP mapping. Bottom, tiled RT-qPCR mapping of Stau1/2 binding. **(C)** Left panel: diagram of βUTR, ΔUTR, ΔSBS, ΔGRE^{S}, and ΔSBS-GRE mutants. Right panel: Stau1 and Stau2 binding is reduced in mutants lacking the SBS sequence. nRIP pull-downs were performed using Stau1 and 2 antibodies and analyzed by RT-qPCR to assess *Cebpb* mRNA enrichment. **(D)** Analysis of mutants expressed in A549 cells by FISH/CK2α imaging. **(E)** The indicated mutants were expressed in $3T3^{RAS}$ cells and analyzed for C/EBPβ phosphorylation on Ser222. Lysates were immunoprecipitated using the p-Ser222 antibody followed by immunoblotting for total C/EBPβ. **(F-G)** The same cells were analyzed for senescence (SA-βGal) **(F)** and expression of SASP genes **(G)**.

Figure 6. *p19$^{Arf-/-}$;Cebpb-GRE$^{\Delta/\Delta}$* MEFs undergo RAS-induced senescence rather than transformation but do not express the SASP.

(A) HRAS^{G12V}-induced phosphorylation on C/EBPβ Ser222 is enhanced in *p19$^{Arf-/-}$;GRE$^{Δ/Δ}$* MEFs. Nuclear lysates from *p19$^{Arf-/-}$* and *p19$^{Arf-/-}$;GRE$^{Δ/Δ}$* MEFs (± HRAS^{G12V}) were analyzed by IP with p-Ser222 antibody followed by immunoblotting for total C/EBPβ. **(B)** Focus assays of cells described in **(A)**. Each open circle (○) represents an independent MEF population (n = 2). **(C)** Senescence of *WT*, *GRE$^{Δ/Δ}$*, *p19$^{Arf-/-}$* and *p19$^{Arf-/-}$;GRE$^{Δ/Δ}$* MEFs ± HRAS^{G12V}. Senescence was measured as the percentage of SA-βGal positive cells (n>400) in 4-6 independent MEF populations. **(D)** *p19$^{Arf-/-}$;GRE$^{Δ/Δ}$* MEFs only weakly express canonical proinflammatory SASP genes but efficiently induce *S100a9*. RNA samples from *WT*, *p19$^{Arf-/-}$*, and *p19$^{Arf-/-}$;GRE$^{Δ/Δ}$* MEFs (± HRAS^{G12V}) were analyzed by RT-qPCR for a panel of SASP genes.

Figure 7. *Cebpb-GRE$^{Δ/Δ}$* mice display reduced progression to adenocarcinoma in a *Kras^{G12D}*-driven model of lung cancer.

(A) Kaplan-Meier curves of *Kras$^{LA2/+}$*and *Kras$^{LA2/+}$;GRE$^{Δ/Δ}$* mice show no significant difference in survival (Log-rank test; p = 0.84). **(B)** Left panel: two representatives H&E images from tumor-bearing lungs in *Kras$^{LA2/+}$*and *Kras$^{LA2/+}$;GRE$^{Δ/Δ}$* mice. Right panel: total lung tumor burdens (percent tumor area/animal) at clinical sacrifice. Tumor areas were determined using the HALO random forest tissue classifier. **(C)** Most severe tumor grades in *Kras$^{LA2/+}$*and *Kras$^{LA2/+}$;GRE$^{Δ/Δ}$* mice as determined by pathological examination of lesions (percent animals in each group; Fisher's exact test; p = 0.0016). **(D)** Left panel: two representative HALO AI segmentations overlaid on H&E images from *WT* and *GRE$^{Δ/Δ}$* lungs (same specimens shown in panel B). HALO AI identifies and segments normal tissue (green), adenomas (yellow) and adenocarcinomas (red). Right panel: HALO AI quantification of adenoma (top) and adenocarcinoma (bottom) graphed as percent lesion area per animal. **(E)** Frequency distribution of nuclear area (log_{10} scale) in adenomas (AD) and adenocarcinomas (ADC) of both genotypes. The total number of nuclei analyzed by HALO are: *Kras^{LA2}* ADC (n = 1,834,153); *Kras^{LA2};GRE$^{Δ/Δ}$* ADC (n = 498,806); *Kras^{LA2}* AD (n = 494,181); *Kras^{LA2};GRE$^{Δ/Δ}$* AD (n = 380,307).

Figure 1

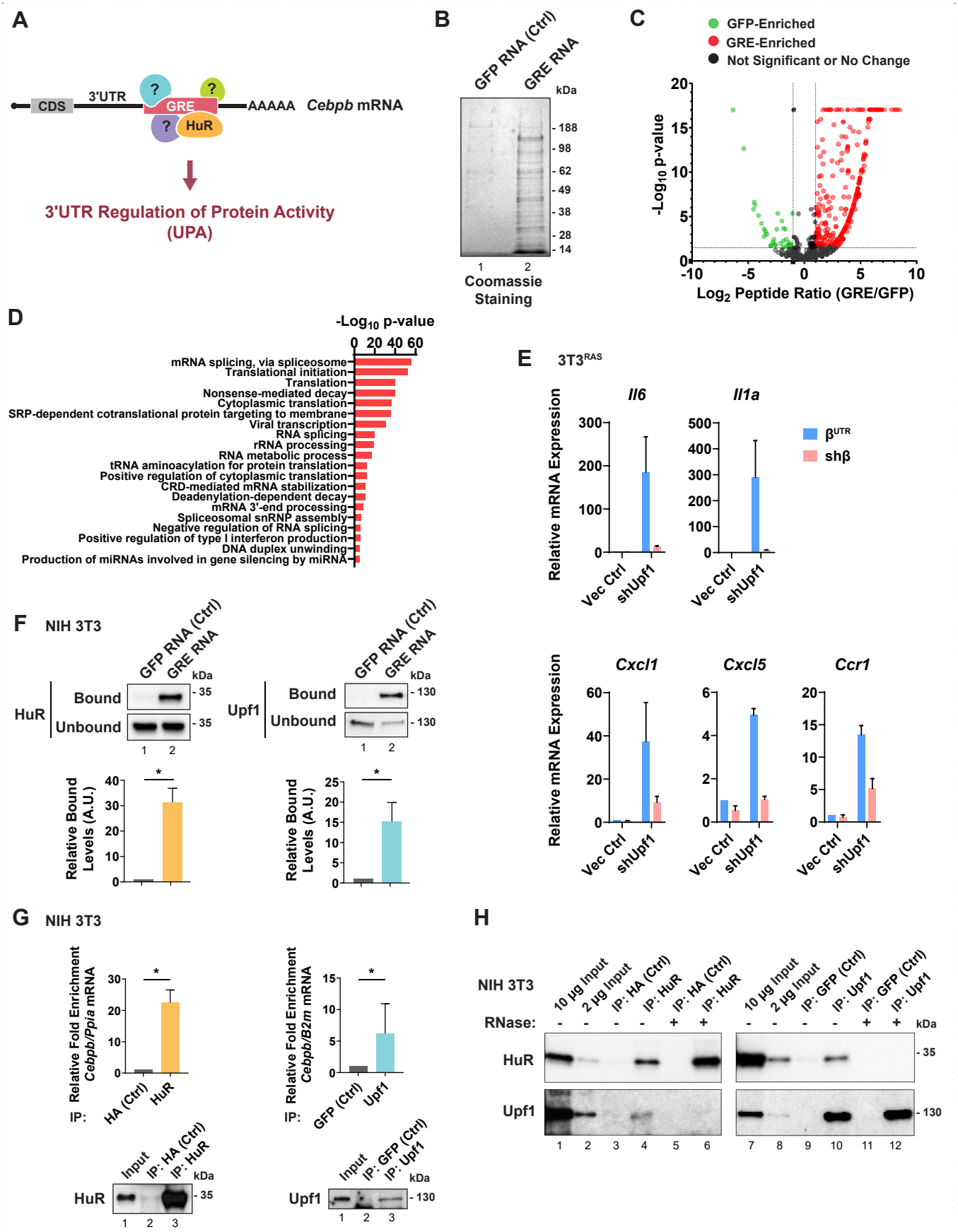
A
CDS
3'UTR
GRE
HuR
AAAAA
Cebpb mRNA
3'UTR Regulation of Protein Activity (UPA)
B
GFP RNA (Ctrl)
GRE RNA
kDa
188
98
62
49
38
28
14
1
2
Coomassie Staining
C
GFP-Enriched
GRE-Enriched
Not Significant or No Change
-Log10 p-value
Log2 Peptide Ratio (GRE/GFP)
D
-Log10 p-value
mRNA splicing, via spliceosome
Translational initiation
Translation
Nonsense-mediated decay
Cytoplasmic translation
SRP-dependent cotranslational protein targeting to membrane
Viral transcription
RNA splicing
rRNA processing
RNA metabolic process
tRNA aminoacylation for protein translation
Positive regulation of cytoplasmic translation
CRD-mediated mRNA stabilization
Deadenylation-dependent decay
mRNA 3'-end processing
Spliceosomal snRNP assembly
Negative regulation of RNA splicing
Positive regulation of type I interferon production
DNA duplex unwinding
Production of miRNAs involved in gene silencing by miRNA
E
3T3RAS
Il6
Il1a
βUTR
shβ
Relative mRNA Expression
Vec Ctrl
shUpf1
Cxcl1
Cxcl5
Ccr1
F
NIH 3T3
GFP RNA (Ctrl)
GRE RNA
HuR
Bound
Unbound
Upf1
Relative Bound Levels (A.U.)
G
NIH 3T3
Relative Fold Enrichment Cebpb/Ppia mRNA
Relative Fold Enrichment Cebpb/B2m mRNA
IP:
HA (Ctrl)
HuR
GFP (Ctrl)
Upf1
Input
IP: HA (Ctrl)
IP: HuR
IP: GFP (Ctrl)
IP: Upf1
H
NIH 3T3
10 µg Input
2 µg Input
IP: HA (Ctrl)
IP: HuR
IP: GFP (Ctrl)
IP: Upf1
RNase:
HuR
Upf1

Figure 2

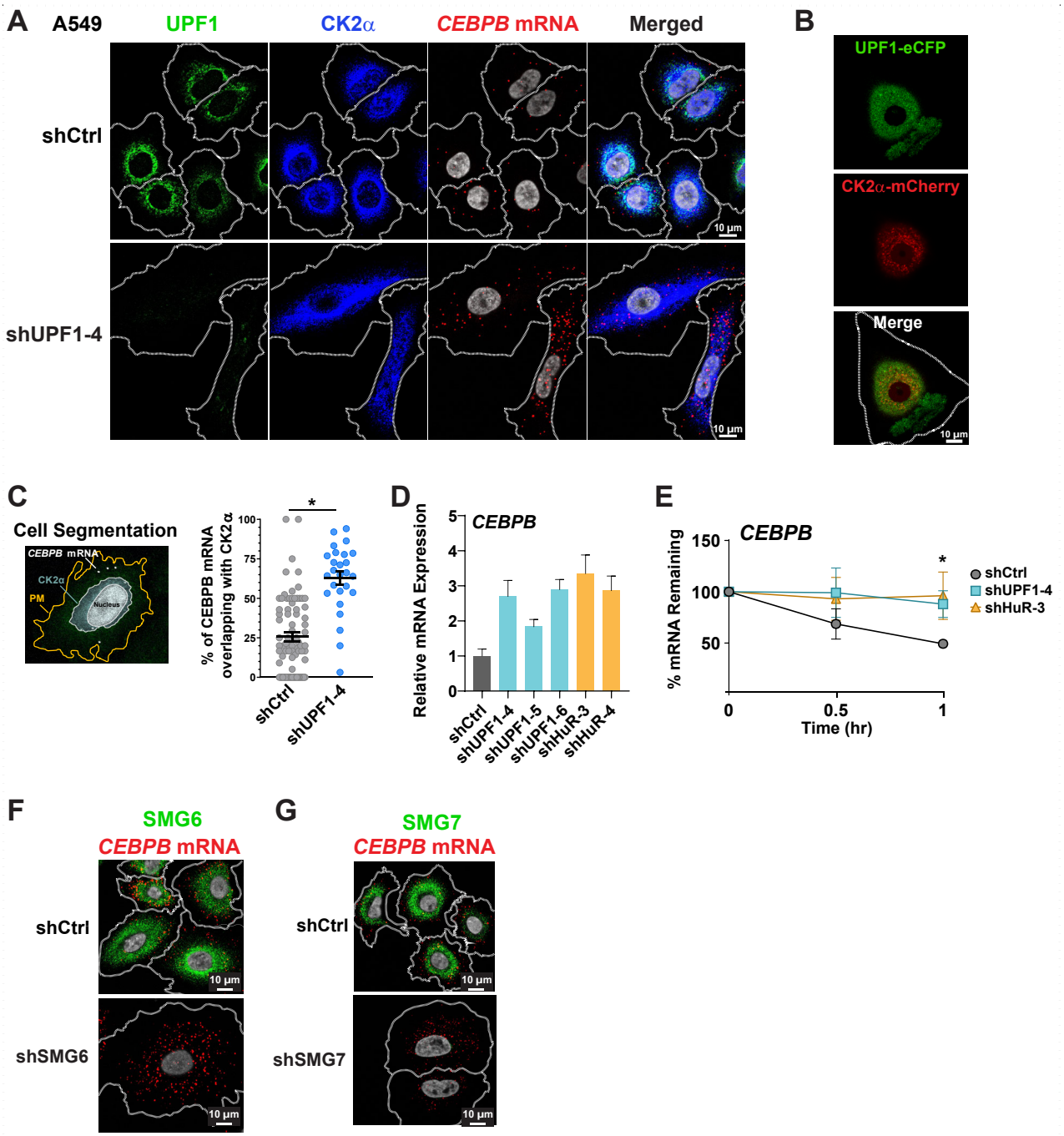
A
A549
UPF1
CK2α
CEBPB mRNA
Merged
shCtrl
shUPF1-4
10 µm
B
UPF1-eCFP
CK2α-mCherry
Merge
C
Cell Segmentation
CEBPB mRNA
CK2α
PM
Nucleus
% of CEBPB mRNA overlapping with CK2α
shCtrl
shUPF1-4
D
CEBPB
Relative mRNA Expression
shCtrl
shUPF1-4
shUPF1-5
shUPF1-6
shHuR-3
shHuR-4
E
CEBPB
% mRNA Remaining
Time (hr)
shCtrl
shUPF1-4
shHuR-3
F
SMG6
CEBPB mRNA
shCtrl
shSMG6
G
SMG7
CEBPB mRNA
shCtrl
shSMG7

Figure 3

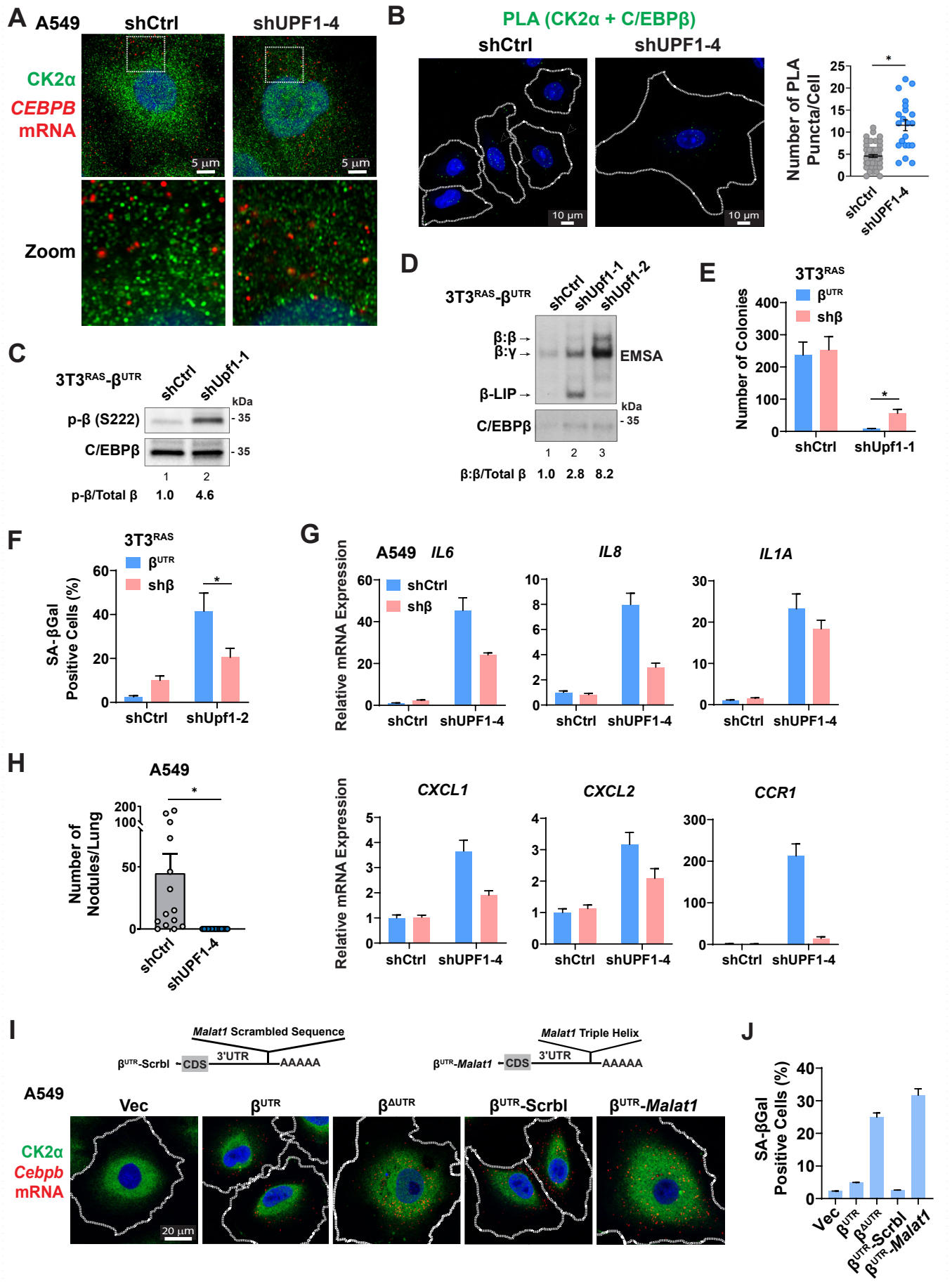
A
A549
shCtrl
shUPF1-4
CK2α
CEBPB mRNA
5 µm
Zoom
B
PLA (CK2α + C/EBPβ)
shCtrl
shUPF1-4
10 µm
Number of PLA Puncta/Cell
shCtrl
shUPF1-4
C
3T3RAS-βUTR
shCtrl
shUpf1-1
kDa
p-β (S222)
C/EBPβ
- 35
p-β/Total β 1.0 4.6
D
3T3RAS-βUTR
shCtrl
shUpf1-1
shUpf1-2
β:β
β:γ
EMSA
β-LIP
C/EBPβ
kDa
- 35
β:β/Total β 1.0 2.8 8.2
E
3T3RAS
βUTR
shβ
Number of Colonies
shCtrl
shUpf1-1
F
3T3RAS
βUTR
shβ
SA-βGal Positive Cells (%)
shCtrl
shUpf1-2
G
A549
IL6
IL8
IL1A
shCtrl
shβ
Relative mRNA Expression
shCtrl
shUPF1-4
H
A549
Number of Nodules/Lung
shCtrl
shUPF1-4
CXCL1
CXCL2
CCR1
Relative mRNA Expression
shCtrl
shUPF1-4
I
Malat1 Scrambled Sequence
βUTR-Scrbl
CDS
3'UTR
AAAAA
Malat1 Triple Helix
βUTR-Malat1
A549
Vec
βUTR
βΔUTR
βUTR-Scrbl
βUTR-Malat1
CK2α
Cebpb mRNA
20 µm
J
SA-βGal Positive Cells (%)
Vec
βUTR
βΔUTR
βUTR-Scrbl
βUTR-Malat1

Figure 4

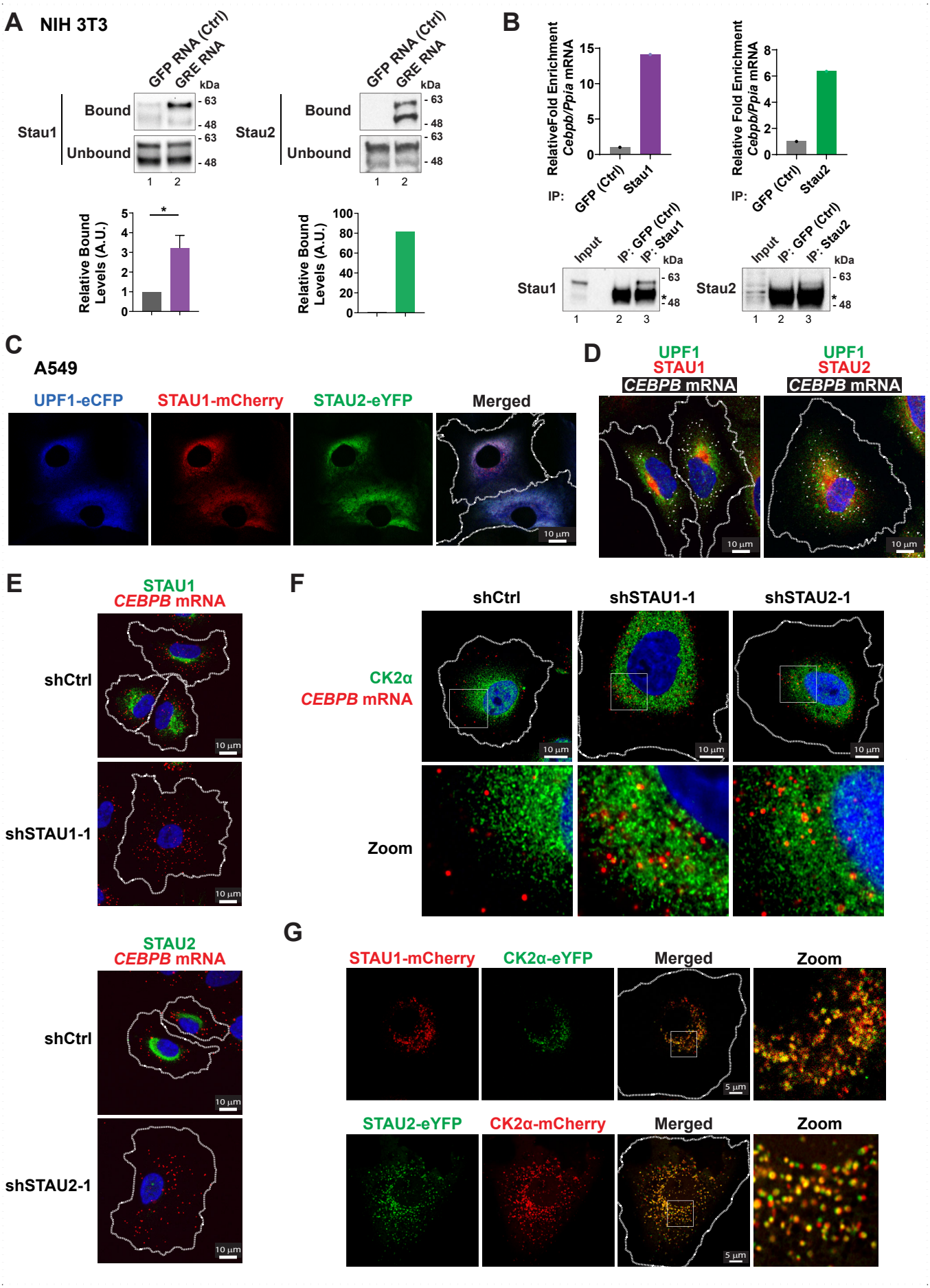
A
NIH 3T3
GFP RNA (Ctrl)
GRE RNA
kDa
Stau1
Bound
Unbound
Stau2
Relative Bound Levels (A.U.)
B
RelativeFold Enrichment Cebpb/Ppia mRNA
Relative Fold Enrichment Cebpb/Ppia mRNA
IP:
GFP (Ctrl)
Stau1
Stau2
Input
IP: GFP (Ctrl)
IP: Stau1
IP: Stau2
C
A549
UPF1-eCFP
STAU1-mCherry
STAU2-eYFP
Merged
10 µm
D
UPF1
STAU1
CEBPB mRNA
STAU2
E
shCtrl
shSTAU1-1
shSTAU2-1
F
shCtrl
shSTAU1-1
shSTAU2-1
CK2α
CEBPB mRNA
Zoom
G
STAU1-mCherry
CK2α-eYFP
Merged
Zoom
STAU2-eYFP
CK2α-mCherry
5 µm

Figure 5

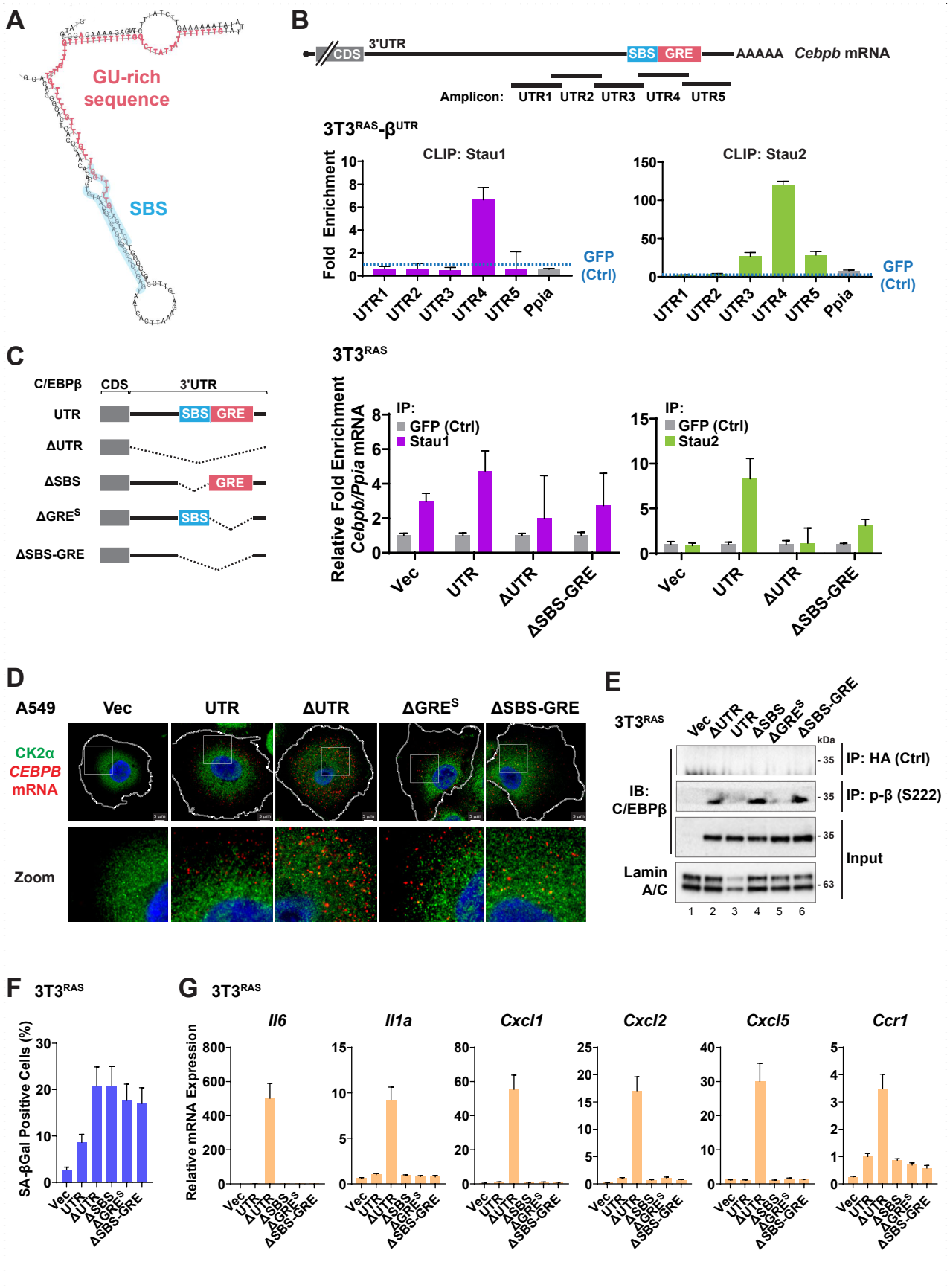
A
GU-rich sequence
SBS
B
CDS
3'UTR
SBS
GRE
AAAAA
Cebpb mRNA
Amplicon: UTR1 UTR2 UTR3 UTR4 UTR5
3T3RAS-βUTR
CLIP: Stau1
CLIP: Stau2
Fold Enrichment
GFP (Ctrl)
UTR1 UTR2 UTR3 UTR4 UTR5 Ppia
C
C/EBPβ
CDS
3'UTR
UTR
ΔUTR
ΔSBS
ΔGRES
ΔSBS-GRE
3T3RAS
Relative Fold Enrichment Cebpb/Ppia mRNA
IP:
GFP (Ctrl)
Stau1
Stau2
Vec
UTR
ΔUTR
ΔSBS-GRE
D
A549
Vec
UTR
ΔUTR
ΔGRES
ΔSBS-GRE
CK2α
CEBPB mRNA
Zoom
E
3T3RAS
Vec ΔUTR UTR ΔSBS ΔGRES ΔSBS-GRE
kDa
IP: HA (Ctrl)
IP: p-β (S222)
Input
IB: C/EBPβ
Lamin A/C
1 2 3 4 5 6
F
3T3RAS
SA-βGal Positive Cells (%)
G
3T3RAS
Il6
Il1a
Cxcl1
Cxcl2
Cxcl5
Ccr1
Relative mRNA Expression

Figure 6

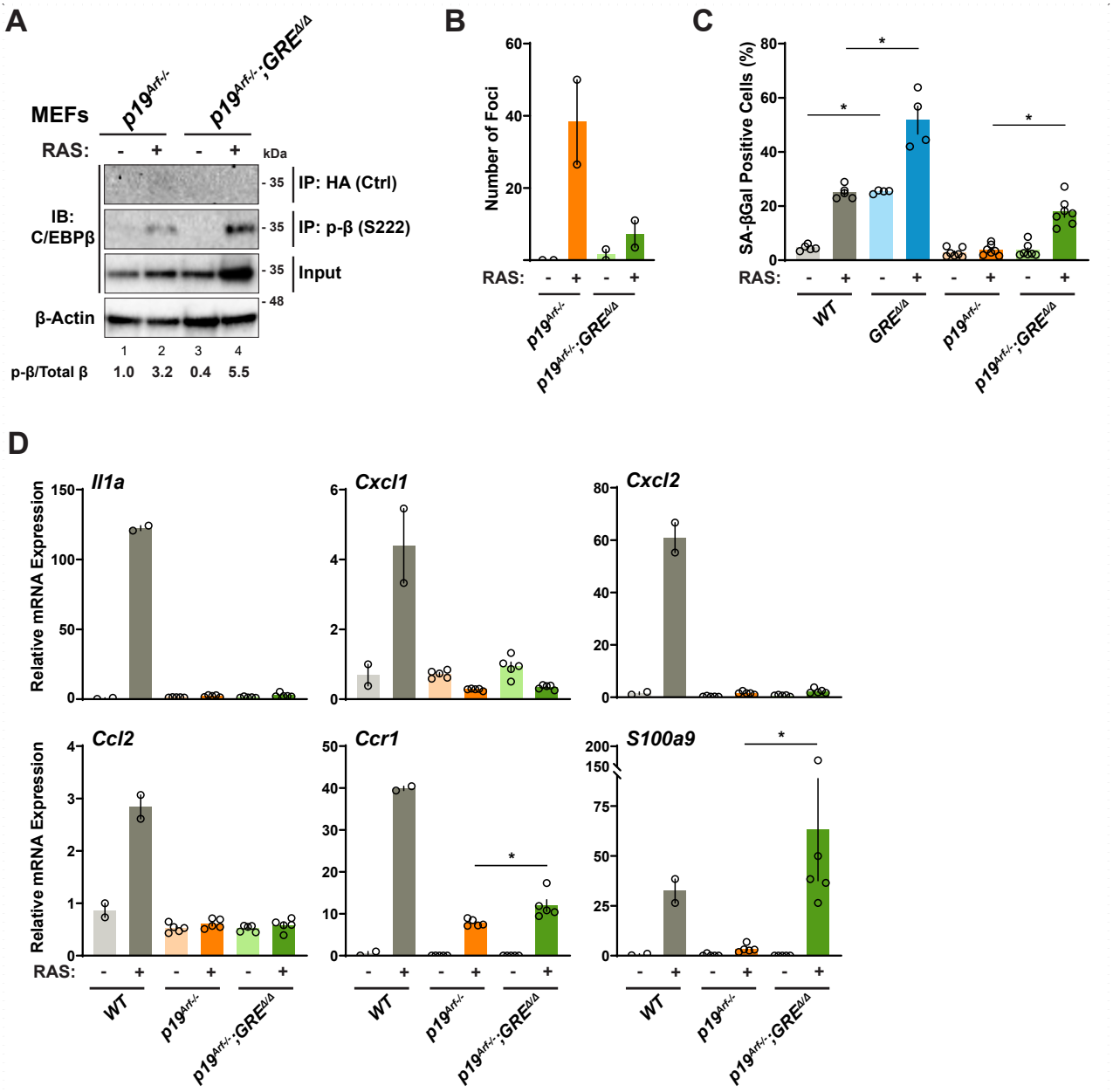
A
MEFs
p19Arf-/-
p19Arf-/-;GREΔ/Δ
RAS: - + - +
kDa
IB: C/EBPβ
IP: HA (Ctrl)
IP: p-β (S222)
Input
β-Actin
35
48
1 2 3 4
p-β/Total β 1.0 3.2 0.4 5.5
B
Number of Foci
RAS: - + - +
p19Arf-/-
p19Arf-/-;GREΔ/Δ
C
SA-βGal Positive Cells (%)
RAS: - + - + - + - +
WT
GREΔ/Δ
p19Arf-/-
p19Arf-/-;GREΔ/Δ
D
Il1a
Cxcl1
Cxcl2
Ccl2
Ccr1
S100a9
Relative mRNA Expression
RAS: - + - + - +
WT
p19Arf-/-
p19Arf-/-;GREΔ/Δ

Figure 7

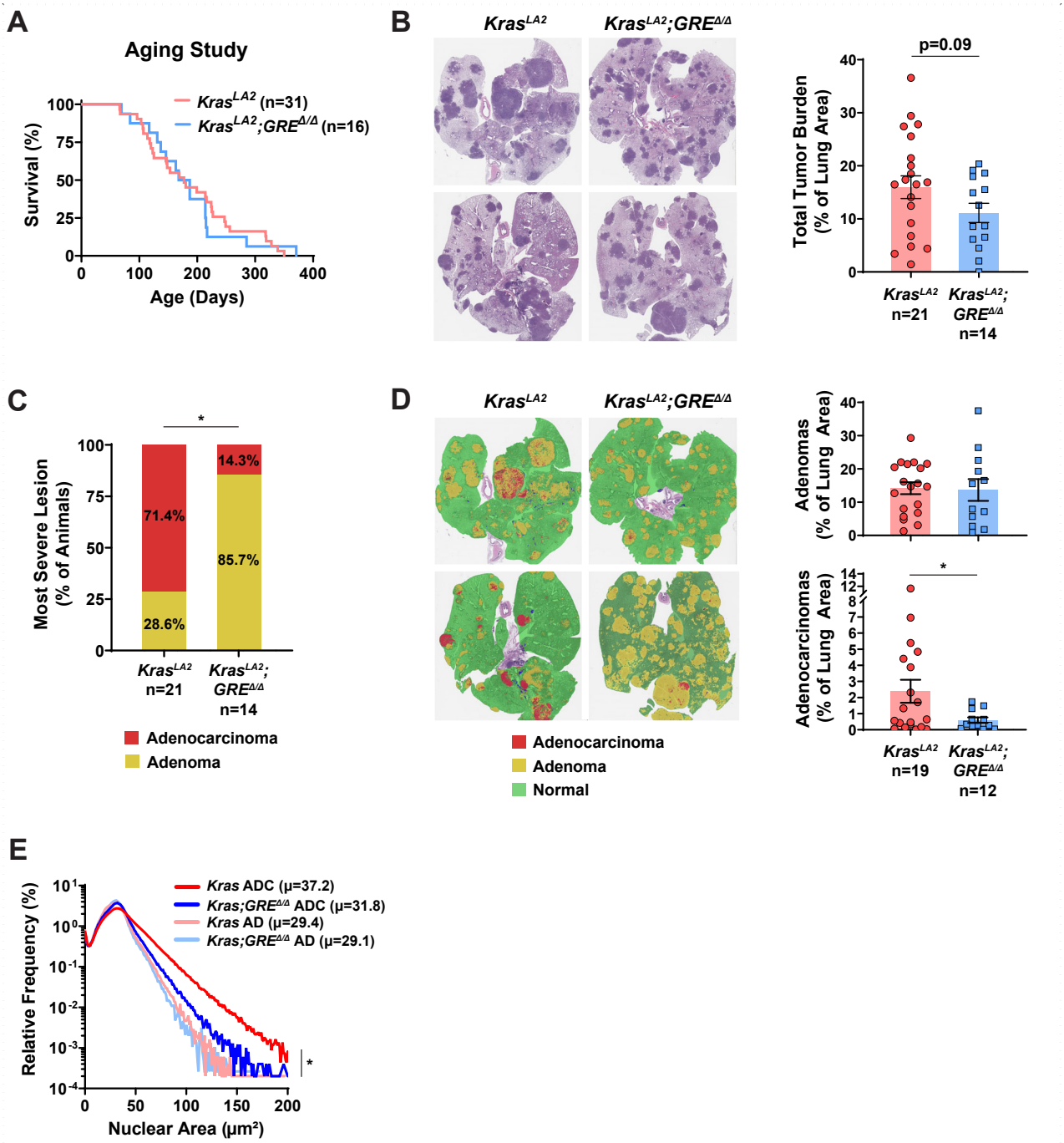
A
Aging Study
Survival (%)
Age (Days)
Kras^LA2 (n=31)
Kras^LA2;GRE^Δ/Δ (n=16)
B
Kras^LA2
Kras^LA2;GRE^Δ/Δ
Total Tumor Burden (% of Lung Area)
p=0.09
Kras^LA2 n=21
Kras^LA2; GRE^Δ/Δ n=14
C
Most Severe Lesion (% of Animals)
71.4%
28.6%
14.3%
85.7%
Adenocarcinoma
Adenoma
D
Adenomas (% of Lung Area)
Adenocarcinomas (% of Lung Area)
Kras^LA2 n=19
Kras^LA2; GRE^Δ/Δ n=12
Normal
E
Relative Frequency (%)
Nuclear Area (μm²)
Kras ADC (μ=37.2)
Kras;GRE^Δ/Δ ADC (μ=31.8)
Kras AD (μ=29.4)
Kras;GRE^Δ/Δ AD (μ=29.1)